# ELSEVIER

#### Contents lists available at ScienceDirect

# International Journal of Solids and Structures





# Computational Cosserat periporomechanics for strain localization and cracking in deformable porous media

Xiaoyu Song\*, Hossein Pashazad

Engineering School of Sustainable Infrastructure & Environment, University of Florida, Gainesville, FL 32611, USA

#### ARTICLE INFO

#### Keywords: Cosserat Periporomechanics Shear banding Cracking Porous media

#### ABSTRACT

Strain localization and cracking in porous media are significant issues in engineering and science. Periporomechanics is a strong nonlocal framework for modeling the mechanics and physics of porous media
with evolving discontinuities. In periporomechanics, the horizon that usually lacks a physical meaning serves
as a nonlocal parameter. In this article, as a new contribution, we formulate a Cosserat periporomechanics
paradigm incorporating a micro-structure related length scale for modeling shear banding and cracking in
dry porous media. In this new Cosserat-periporomechanics framework, each material point is endowed with
both translational and rotational degrees of freedom following the Cosserat continuum theory. We formulate
a stabilized Cosserat constitutive correspondence principle through which classical micro-polar constitutive
models for porous media can be used in Cosserat periporomechanics. We have numerically implemented the
Cosserat periporomechanics paradigm through an explicit Lagrangian meshfree algorithm. We first present
numerical examples to validate the implemented computational Cosserat periporomechanics paradigm for
modeling shear bands and cracks. We then present numerical examples to demonstrate the efficacy and
robustness of the Cosserat periporomechanics for modeling the shear banding bifurcation and crack branching
in dry porous media.

#### 1. Introduction

Strain localization and cracking in porous media are significant in engineering and science (e.g., Terzaghi and Peck, 1948; Lewis et al., 1998; Zienkiewicz et al., 1999; Cheng, 2016). For instance, shear banding in geomaterials can significantly compromise the integrity of geo-infrastructure (Terzaghi and Peck, 1948; Coussy, 2004). Knowledge of cracking in porous media is instrumental in predicting and mitigating reservoir-related hazards and enhancing oil and gas harvest in porous geological formations (e.g., Zoback, 2010; Pollard and Fletcher, 2005; Sun et al., 2021a,b). Poromechanics is an essential tool to study the mechanics and physics including shear banding and cracking in porous media (Lewis et al., 1998; Zienkiewicz et al., 1999). Periporomechanics is a strong non-local reformulation of classical poromechanics (Coussy, 2004; Cheng, 2016) for modeling the mechanics and physics of variably saturated porous media with evolving discontinuities (e.g., Song and Menon, 2019; Song and Khalili, 2019; Song and Silling, 2020; Menon and Song, 2021a,b, 2022a,c,b). In line with the peridynamics for solids (Silling, 2000; Silling et al., 2007; Madenci and Oterkus, 2014), the motion equation and mass balance equations of periporomechanics are in the form of integrodifferential equations (integration in space and difference in time) through the peridynamic (PD) state and effective

force state concept (Silling et al., 2007; Song and Silling, 2020). This salient feature of periporomechanics makes it a legitimate numerical tool for modeling discontinuities and progressive failure in deformable porous media such as shear bands and cracks. It is noted that the previous periporomechanics was developed for non-polar porous materials in which material points have two kinds of degrees of freedom, i.e., translational displacement and pore fluid pressure. It is known that shear bands in porous media such as soils have a finite thickness on the order of several particle sizes and involve particle rotations in the banded deformation zone (e.g., Mühlhaus and Vardoulakis, 1987; Sulem and Vardoulakis, 1995). Meanwhile, in periporomechanics the horizon that serves as a non-local parameter usually lacks a direct relation to the micro-structure of deformable porous media (e.g., soils). Therefore, the formulation of a visco-Cosserat periporomechanics paradigm can contribute to realistically modeling shear bands and cracking in porous media.

In this article, as a new contribution, we formulate a Cosserat periporomechanics paradigm incorporating a micro-structure based length scale for modeling shear banding and cracking in dry porous media. The viscosity is included to study the rate dependency of shear banding and cracking in porous media (e.g, Terzaghi and Peck, 1948; Taylor,

E-mail address: xysong@ufl.edu (X. Song).

<sup>\*</sup> Corresponding author.

1948; Lambe and Whitman, 1991; Terzaghi et al., 1996). In this micropolar periporomechanics framework, each material point under the dry condition has translational and rotational degrees of freedom. It is noted that the Cosserat continuum theory has been successfully applied for modeling shear bands in porous media using the classical finite element method while mitigating its pathological issue (e.g., De Borst, 1991; De Borst and Sluys, 1991; Tang et al., 2021, 2022). We refer to the distinguished literature on this subject (e.g., de Borst, 1993; Sulem and Vardoulakis, 1995). Cosserat continuum theory has also been used in peridynamics (PD) for modeling the mechanical behavior of solids (e.g., Gerstle, 2015; Chowdhury et al., 2015, and among others). For instance, in Gerstle (2015) a micropolar PD formulation following standard Cauchy elasticity was proposed for modeling brittle materials like concrete. The extended bond-based PD model that incorporates the bond rotation has been proposed to model fracture problems in brittle materials (Zhu and Ni, 2017; Li et al., 2020). We note that the bondrotation enhancement proposed in those studies has been focused on remedying the limitation of Poisson's ratio (i.e., one quarter) in the original bond-based PD framework (Silling, 2000). In Chowdhury et al. (2015), a micropolar state-based PD framework was formulated for modeling cracks in which a standard correspondence material model was proposed. It is noted that the framework in Chowdhury et al. (2015) is limited for isotropic elastic materials. It is known that porous media could show a rate dependency (e.g., viscosity) in the process of shear banding and cracking (e.g., fault creep) (Sleep and Blanpied, 1992; Steinbrugge et al., 1960; Noda and Lapusta, 2013). In this study, as an original contribution, we develop a visco-Cosserat periporomechanics framework for dry porous media. This new framework incorporates a physics-based material length scale (i.e., Cosserat length scale) and rate-dependency for more realistic modeling of progressive localized failure and cracking of porous media under dry conditions.

We note that no PD material model in the periporomechanics framework is available for modeling porous media. Thus, in this new visco-Cosserat periporomechanics framework, the multiphase correspondence principle for non-polar porous media (Song and Silling, 2020; Menon and Song, 2021b) is reformulated to include the rotational degree of freedom. Through the Cosserat multiphase correspondence principle, advanced elastoplastic constitutive models for geomaterials (e.g., Tamagnini et al., 2002; Borja, 2013; Song et al., 2018a) can be reformulated for micro-polar porous media (de Borst, 1993) and then incorporated into the Cosserat periporomechanics paradigm. Nonetheless, the standard Cosserat correspondence principle inherits the zero-energy mode instability from the non-polar constitutive correspondence principle. In this study, we formulate a stabilized Cosserat constitutive correspondence principle to circumvent this issue using the energy method (e.g., Silling, 2017; Menon and Song, 2021b). With this stabilized micro-polar correspondence principle, classical constitutive and data-driven material models (e.g., Song et al. (2018a), Masi et al. (2021)) for porous media can be incorporated into the proposed Cosserat periporomechanics. We refer to Menon and Song (2022c) for a comprehensive review of methods for mitigating zero-energy mode instability associated with the original constitutive correspondence principle in PD for solids. We have numerically implemented the proposed Cosserat periporomechanics paradigm through an explicit Lagrangian meshfree algorithm for dynamic problems (Silling and Askari, 2005; Menon and Song, 2022c; Zienkiewicz et al., 1999; Hughes, 2012; Belytschko et al., 2014). Two numerical examples inspired by experimental works in the literature are presented to test the implemented computational micro-periporomechanics paradigm in modeling shear banding and mode I cracking in porous media. We then present two numerical examples to demonstrate the efficacy and robustness of the Cosserat periporomechanics for modeling the characteristics of shear banding bifurcation (e.g., inclination angle and thickness of the two conjugate shear bands) and dynamic crack branching (e.g., the timing of branching) in dry porous media (i.e., single-phase porous media).

The reminder of this article is organized as follows. Section 2 deals with the mathematical formulation of the visco-Cosserat periporomechanic paradigm that includes the governing equations, the stabilized Cosserat constitutive correspondence principle, and the Cosserat viscoplasticity and visco-elasticity, and a bilinear damage model. Section 3 presents the numerical implementation of the proposed Cosserat periporomechanics paradigm through an explicit Newmark scheme with an augmented energy criterion for numerical stability. Section 4 deals with numerical examples to validate the implemented Cosserat periporomechanics model and demonstrate its efficacy and robustness in modeling shear banding and crack branching in dry porous media. For sign convection, the assumption in continuum mechanics is adopted, i.e., the tensile force and deformation under tension is positive.

#### 2. Mathematical formulation

In this section, we present the mathematical formulation of the Cosserat periporomechanics for dry porous media. First, we present the governing equations of Cosserat periporomechanics for dry porous materials. Second, we develop a Cosserat constitutive correspondence principle through which the classical visco-Cosserat material models can be incorporated into the proposed Cosserat periporomechanics. Third, we present an energy-based stabilization scheme in the Cosserat periporomechanics framework to mitigate the zero-energy mode deformation instability. Finally, the classical Cosserat visco-plasticity, visco-elasticity, and damage models are presented.

#### 2.1. Governing equations of Cosserat periporomechanics

In periporomechanics, a porous material body can be conceptualized as a collection of a finite number of material points with poromechanical and physical interactions at a finite distance. The scope of the present contribution is to formulate visco-Cosserat periporomechanics for a dry porous material. In line with the classical Cosserat continuum theory (e.g., Cosserat and Cosserat, 1909; Malvern, 1969; Sulem and Vardoulakis, 1995; Eringen and Eringen, 1999) in the proposed Cosserat periporomechanics (CPPM) each material point is endowed with translational and rotational degrees of freedom. Let X denote a material point and let X' denote its neighboring material point in the initial configuration. For notations, a state or parameter without a prime is associated with material point X, and a state or parameter with a prime is associated with material point X'. For example, we can define y and y' as the spatial locations of material points X and X' in the deformed configuration. The partial density of a solid skeleton is defined as

$$\rho^s = \phi \rho_s,\tag{1}$$

where  $\phi$  is the volume fraction of the solid skeleton (i.e., one minus porosity) and  $\rho_s$  is the intrinsic density of the solid skeleton. Here, the porosity is the fraction between the pore space and the porous media's total volume.

Fig. 1 plots the kinematics of CPPM for material points. In line with the non-polar PPM, the deformation state and the relative displacement state associated with bond  $\xi = X' - X$  at material point X' read

$$\underline{Y} = \mathbf{y}' - \mathbf{y},\tag{2}$$

$$U = u' - u, (3)$$

where u and u' are the displacement vectors of material points X and X', respectively. It is assumed that material points have no macro rotations. Given the micro-rotations  $\omega$  and  $\omega'$  at X and X', respectively, the micro-rotation state and the mean micro-rotation state associated with bond  $\xi$  at X can be defined as

$$\underline{\Omega} = \omega' - \omega,\tag{4}$$

$$\underline{\underline{\Omega}} = \frac{1}{2}(\boldsymbol{\omega}' + \boldsymbol{\omega}),\tag{5}$$

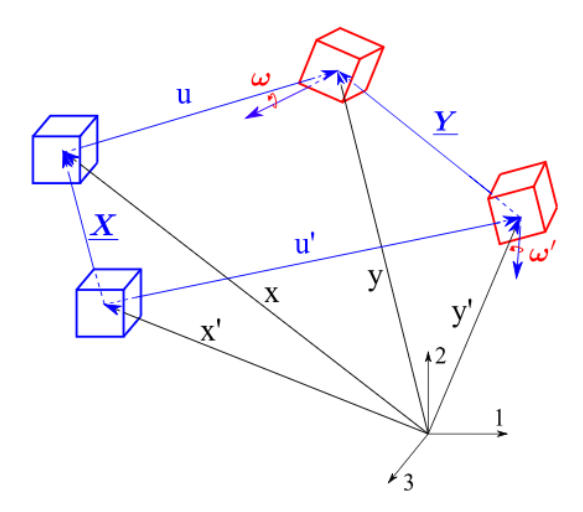


Fig. 1. Kinematics of two material points X and X' in Cosserat periporomechanics.

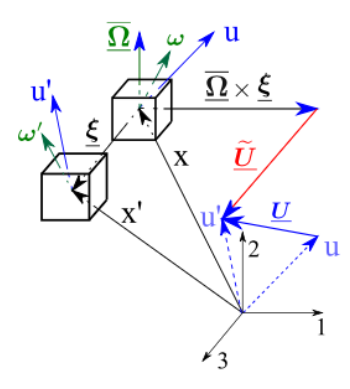


Fig. 2. Schematic of composite states in Cosserat periporomechanics.

Fig. 2 plots the composite state in Cosserat periporomechanics. Referring to Fig. 2, the composite deformation and displacement states in Cosserat periporomechanics can be respectively defined as

$$\widetilde{\underline{Y}} = \underline{Y} - \overline{\underline{\Omega}} \times \underline{X},\tag{6}$$

$$\widetilde{U} = U - \overline{\Omega} \times X,\tag{7}$$

where  $\times$  is the cross product operator of two vectors, and  $\underline{X}=\underline{\xi}$  stands for the bond between material points X and X' in the reference configuration. We note that following the assumption of the small deformation that (6) and (7) can be rewritten as

$$\frac{\widetilde{Y}}{\widetilde{Y}} \approx \underline{Y} - \overline{\underline{\Omega}} \times \underline{Y},\tag{8}$$

$$\widetilde{U} \approx U - \overline{\Omega} \times Y,$$
 (9)

Next, we derive the governing equations from a free energy of a polar porous body following Song and Silling (2020). Assuming no heat flux, the free energy density of the solid skeleton in Cosserat periporomechanics under dry condition (i.e., single phase) can be defined as

$$\overline{W} = \overline{W}(\widetilde{Y}, \Omega).$$
 (10)

Let  $\overline{\mathcal{G}}$  be the effective force state and  $\underline{\mathcal{M}}$  be the moment state. Through Fréchet derivatives (Silling et al., 2007; Song and Silling, 2020), the effective force state and moment state on a Cosserat periporomechanics bond can be defined as

$$\underline{\overline{\mathcal{T}}} = \frac{\partial \overline{\overline{W}}}{\partial \underline{\widetilde{Y}}},\tag{11}$$

$$\underline{\mathcal{M}} = \frac{\partial \overline{\mathcal{W}}}{\partial \Omega}.$$
 (12)

Then, the variational form of the free energy of the solid skeleton can be written as

$$\Delta \overline{W} = \frac{\partial \overline{W}}{\partial \underline{\widetilde{Y}}} \cdot \Delta \underline{\widetilde{Y}} + \frac{\partial \overline{W}}{\partial \underline{\Omega}} \cdot \Delta \underline{\Omega} 
= \overline{\mathcal{F}} \cdot \Delta \widetilde{Y} + \mathcal{M} \cdot \Delta \Omega,$$
(13)

where • is the inner product of vector states (Silling et al., 2007).

From (8) the variational form of the composite deformation state  $\underline{\widetilde{Y}}$ 

$$\underline{\Delta \widetilde{Y}} = \underline{\Delta Y} - \underline{\Delta \widetilde{\Omega}} \times \underline{Y} - \underline{\Delta \widetilde{\Omega}} \times \underline{\Delta Y}$$

$$= \underline{\Delta Y} - \underline{\Delta \widetilde{\Omega}} \times Y \tag{14}$$

where the second-order term on the second line is omitted following the small deformation assumption. It follows from (14) that Eq. (13) can be written as

$$\Delta \overline{W} = \overline{\mathcal{T}} \cdot \left( \Delta \underline{Y} - \Delta \underline{\Omega} \times \underline{Y} \right) + \underline{\mathcal{M}} \cdot \Delta \underline{\Omega}. \tag{15}$$

The total energy  $\mathcal{W}$  (i.e., the summation of the potential energy and kinetic energy) of a bounded single-phase porous body  $\mathcal{B}$  can be written as

$$\mathcal{W} = \int_{\omega} \overline{\mathcal{W}} - \rho^{s} \mathbf{g} \cdot \mathbf{y} - \mathbf{l} \cdot \boldsymbol{\omega} + \rho^{s} \ddot{\boldsymbol{u}} \cdot \mathbf{y} + \mathcal{F}^{s} \ddot{\boldsymbol{\omega}} \cdot \boldsymbol{\omega} \, dV, \tag{16}$$

where  $\rho^s$  is partial density of the solid skeleton as defined in (1), g is gravity acceleration, l is body couple density,  $\dot{u}$  is velocity, and  $\mathcal{F}^s$  is the micro-inertia of the solid skeleton. Note that the kinetic energy is considered through inertial loads (Malvern, 1969).

Next, we derive the equilibrium equation of the Cosserat periporomechanics for a dry porous body from (16). The first-order variational form of  $\mathcal{W}$  can be written as

$$0 = \int_{\mathcal{R}} \left[ \overline{\mathcal{F}} \bullet (\Delta \underline{Y} - \Delta \overline{\Omega} \times \underline{Y}) + \underline{\mathcal{M}} \bullet \Delta \underline{\Omega} - \rho^{s} \mathbf{g} \cdot \Delta \mathbf{y} - \mathbf{l} \cdot \Delta \boldsymbol{\omega} \right.$$

$$\left. + \rho^{s} \mathbf{i} \mathbf{i} \cdot \Delta \mathbf{y} + \mathcal{F}^{s} \ddot{\boldsymbol{\omega}} \cdot \Delta \boldsymbol{\omega} \right] dV$$

$$= \int_{\mathcal{R}} \left[ \int_{\mathcal{R}} \overline{\mathcal{F}} \cdot (\Delta \mathbf{y}' - \Delta \mathbf{y}) dV' + \int_{\mathcal{R}} \overline{\mathcal{F}}' \times \underline{Y} \cdot \left( \frac{\Delta \boldsymbol{\omega}' + \Delta \boldsymbol{\omega}}{2} \right) dV' \right.$$

$$\left. + \int_{\mathcal{R}} \underline{\mathcal{M}} \cdot (\Delta \boldsymbol{\omega}' - \Delta \boldsymbol{\omega}) dV' - \rho^{s} \mathbf{g} \cdot \Delta \mathbf{y} - \mathbf{l} \cdot \Delta \boldsymbol{\omega} + \rho^{s} \mathbf{i} \mathbf{i} \cdot \Delta \mathbf{y} \right.$$

$$\left. + \mathcal{F}^{s} \ddot{\boldsymbol{\omega}} \cdot \Delta \boldsymbol{\omega} \right] dV. \tag{17}$$

By interchanging the dummy variable  $X \longleftrightarrow X'$  (Song and Silling, 2020) in the first, third and fifth terms in the integrand of (17) leads to

$$0 = \int_{\mathcal{B}} \left[ \int_{\mathcal{H}} \left( \overline{\underline{\mathcal{T}}}' - \overline{\underline{\mathcal{T}}} \right) dV' \cdot \Delta \mathbf{y} + \frac{1}{2} \int_{\mathcal{H}} \underline{Y} \times \left( \overline{\underline{\mathcal{T}}}' - \overline{\underline{\mathcal{T}}} \right) dV' \cdot \Delta \boldsymbol{\omega} \right. \\ + \int_{\mathcal{H}} \left( \underline{\mathcal{M}}' - \underline{\mathcal{M}} \right) dV' \cdot \Delta \boldsymbol{\omega} - \rho^{s} \mathbf{g} \cdot \Delta \mathbf{y} - \mathbf{l} \cdot \Delta \boldsymbol{\omega} + \rho^{s} \ddot{\mathbf{u}} \cdot \Delta \mathbf{y} \\ + \left. \mathcal{F}^{s} \ddot{\boldsymbol{\omega}} \cdot \Delta \boldsymbol{\omega} \right] dV.$$
 (18)

Note that Eq. (18) must hold for any  $\Delta y$  and  $\Delta \omega$  which can vary independently. Thus, it follows from this requirement and the assumption of small deformation that we have

$$0 = \int_{\mathscr{Z}} \left( \overline{\mathscr{Z}}' - \overline{\mathscr{Z}} \right) dV' - \rho^s \mathbf{g} + \rho^s \ddot{\mathbf{u}}, \tag{19}$$

$$0 = \int_{\mathcal{Z}} \left( \underline{\mathcal{M}}' - \underline{\mathcal{M}} \right) dV' + \frac{1}{2} \int_{H} \underline{Y} \times \left( \overline{\underline{\mathcal{T}}}' - \overline{\underline{\mathcal{T}}} \right) dV' - I + \mathcal{F}^{s} \ddot{\boldsymbol{\omega}}. \tag{20}$$

It follows from (19) and (20) that the equations of motion and rotation in Cosserat periporomechanics under the dry condition can be written as

$$\rho^{s}\ddot{\boldsymbol{u}} = \int_{\mathscr{X}} \left( \overline{\mathscr{Z}} - \overline{\mathscr{Z}}' \right) dV' + \rho^{s} \boldsymbol{g}, \tag{21}$$

$$\mathcal{F}^{s}\ddot{\boldsymbol{\omega}} = \int_{\mathcal{L}} \left( \underline{\mathcal{M}} - \underline{\mathcal{M}'} \right) dV' + \frac{1}{2} \int_{\mathcal{L}} \underline{Y} \times \left( \underline{\overline{\mathcal{T}}} - \underline{\overline{\mathcal{T}}'} \right) dV' + I. \tag{22}$$

Note that in (22)  $\mathcal{I}^{s}\ddot{\omega}$  represents the angular momentum of a spinning material point (Sulem and Vardoulakis, 1995).

To complete Eqs. (21) and (22), we need to introduce the constitutive models for the effective force state and the moment state. In this article, as a new contribution we develop a stabilized Cosserat correspondence principle through which classical local constitutive models for micro-polar porous media can be incorporated into the proposed Cosserat periporomechanics. In what follows, we derive the Cosserat correspondence principle through an equivalence of internal energy between local micro-polar poromechanics and Cosserat periporomechanics.

# 2.2. Cosserat periporomechanics correspondence principle

This part deals with the Cosserat correspondence principle following the lines in non-polar periporomechanics (Song and Silling, 2020). To achieve this task we first derive an expression of internal energy density for micro-polar porous media in the framework of Cosserat periporomechanics By ignoring the heat source and/or heat flux, let us multiply (21) by  $\dot{u}$  and integrate over a finite sub-region  $\mathcal{P}$  within bounded micro-polar porous body  $\mathcal{B}$ , and we have

$$\int_{\mathcal{D}} \rho^{s} \dot{\mathbf{u}} \cdot \dot{\mathbf{u}} dV = \int_{\mathcal{D}} \int_{\mathcal{D}} \left( \overline{\mathcal{D}} - \overline{\mathcal{D}}' \right) \cdot \dot{\mathbf{u}} dV' dV + \int_{\mathcal{D}} \rho^{s} \mathbf{g} \cdot \dot{\mathbf{u}} dV. \tag{23}$$

Similarly, multiply (22) by  $\dot{\omega}$  and integrate over  $\mathcal{P}$ , and we have

$$\int_{\mathcal{P}} \mathcal{F}^{s} \ddot{\boldsymbol{\omega}} \cdot \dot{\boldsymbol{\omega}} dV = \int_{\mathcal{P}} \int_{\mathcal{R}} \left( \underline{\mathcal{M}} - \underline{\mathcal{M}'} \right) \cdot \dot{\boldsymbol{\omega}} dV' dV + \int_{\mathcal{P}} \boldsymbol{l} \cdot \dot{\boldsymbol{\omega}} dV \\
+ \frac{1}{2} \int_{\mathcal{P}} \int_{\mathcal{R}} \underline{Y} \times \left( \underline{\overline{\mathcal{T}}} - \underline{\overline{\mathcal{T}'}} \right) \cdot \dot{\boldsymbol{\omega}} dV' dV \tag{24}$$

Summation of (23) and (24) gives the balance of energy as

$$\int_{\mathcal{P}} (\rho^{s} \ddot{\mathbf{u}} \cdot \dot{\mathbf{u}} + \mathcal{F}^{s} \ddot{\boldsymbol{\omega}} \cdot \dot{\boldsymbol{\omega}}) dV = \int_{\mathcal{P}} \int_{\mathcal{R}} \left( \underline{\mathcal{T}} - \underline{\mathcal{T}}' \right) \cdot \dot{\mathbf{u}} dV' dV 
+ \int_{\mathcal{P}} \int_{\mathcal{R}} \left( \underline{\mathcal{M}} - \underline{\mathcal{M}}' \right) \cdot \dot{\boldsymbol{\omega}} dV' dV 
+ \frac{1}{2} \int_{\mathcal{P}} \int_{\mathcal{R}} \underline{Y} \times \left( \underline{\mathcal{T}} - \underline{\mathcal{T}}' \right) \cdot \dot{\boldsymbol{\omega}} dV' dV 
+ \int_{\mathcal{P}} (\rho^{s} \mathbf{g} \cdot \dot{\mathbf{u}} + \mathbf{l} \cdot \dot{\boldsymbol{\omega}}) dV.$$
(25)

The first three terms in the right-hand side of (25) can be rewritten as

$$\int_{\mathscr{P}} \int_{\mathscr{X}} \left( \overline{\underline{\mathscr{T}}} - \overline{\underline{\mathscr{T}}}' \right) \cdot \dot{\boldsymbol{u}} \, dV' \, dV = \int_{\mathscr{P}} \int_{\mathscr{B}} \left( \overline{\underline{\mathscr{T}}} \cdot \dot{\boldsymbol{u}}' - \overline{\underline{\mathscr{T}}}' \cdot \dot{\boldsymbol{u}} \right) \, dV' \, dV \\
- \int_{\mathscr{P}} \int_{\mathscr{B}} \overline{\underline{\mathscr{T}}} \left( \dot{\boldsymbol{u}}' - \dot{\boldsymbol{u}} \right) \, dV' \, dV \\
= \int_{\mathscr{P}} \int_{\mathscr{B} \setminus \mathscr{P}} \left( \overline{\underline{\mathscr{T}}} \cdot \dot{\boldsymbol{u}}' - \overline{\underline{\mathscr{T}}}' \cdot \dot{\boldsymbol{u}} \right) \, dV' \, dV \\
- \int_{\mathscr{P}} \int_{\mathscr{D}} \overline{\underline{\mathscr{T}}} \left( \dot{\boldsymbol{u}}' - \dot{\boldsymbol{u}} \right) \, dV' \, dV \tag{26}$$

$$\int_{\mathcal{P}} \int_{\mathcal{H}} \left( \underline{\mathcal{M}} - \underline{\mathcal{M}}' \right) \cdot \dot{\boldsymbol{\omega}} \, dV' \, dV = \int_{\mathcal{P}} \int_{\mathcal{R}} \left( \underline{\mathcal{M}} \cdot \dot{\boldsymbol{\omega}}' - \underline{\mathcal{M}}' \cdot \dot{\boldsymbol{\omega}} \right) \, dV' \, dV \\
- \int_{\mathcal{P}} \int_{\mathcal{R}} \underline{\mathcal{M}} \cdot \left( \dot{\boldsymbol{\omega}}' - \dot{\boldsymbol{\omega}} \right) \, dV' \, dV \\
= \int_{\mathcal{P}} \int_{\mathcal{R} \setminus \mathcal{P}} \left( \underline{\mathcal{M}} \cdot \dot{\boldsymbol{\omega}}' - \underline{\mathcal{M}}' \cdot \dot{\boldsymbol{\omega}} \right) \, dV' \, dV \\
- \int_{\mathcal{P}} \int_{\mathcal{R}} \underline{\mathcal{M}} \cdot \left( \dot{\boldsymbol{\omega}}' - \dot{\boldsymbol{\omega}} \right) \, dV' \, dV \tag{27}$$

$$\begin{split} &\frac{1}{2} \int_{\mathcal{P}} \int_{\mathcal{H}} \underline{Y} \times \left( \underline{\overline{\mathcal{T}}} - \underline{\overline{\mathcal{T}}}' \right) \cdot \dot{\omega} \, dV' dV \\ &= \int_{\mathcal{P}} \int_{\mathcal{R}} \left( \underline{\overline{\mathcal{T}}} \cdot \frac{\dot{\omega}'}{2} \times \underline{Y}' - \underline{\overline{\mathcal{T}}}' \cdot \frac{\dot{\omega}}{2} \times \underline{Y} \right) \, dV' dV \\ &- \int_{\mathcal{P}} \int_{\mathcal{R}} \underline{\mathcal{T}} \cdot \frac{\dot{\omega}' + \dot{\omega}}{2} \times \underline{Y} \, dV' dV \end{split}$$

$$= \int_{\mathscr{P}} \int_{\mathscr{R} \setminus \mathscr{P}} \left( \overline{\mathscr{Z}} \cdot \frac{\boldsymbol{\omega}'}{2} \times \underline{Y}' - \overline{\mathscr{Z}}' \cdot \frac{\boldsymbol{\omega}}{2} \times \underline{Y} \right) dV' dV$$

$$- \int_{\mathscr{P}} \int_{\mathscr{R}} \underline{\mathscr{T}} \cdot \frac{\boldsymbol{\omega}' + \boldsymbol{\omega}}{2} \times \underline{Y} dV' dV$$
(28)

It follows from (25), (26), (27), and (28) that we can express the balance of energy as

$$\hat{\mathcal{R}} + \mathcal{W}_{abs} = \mathcal{W}_{sun},\tag{29}$$

where  $\hat{\mathcal{R}}$  is the rate of kinetic energy,  $W_{abs}$  is absorbed power, and  $W_{sup}$  is supplied power. The three terms are written as

$$\hat{\mathcal{R}} = \int_{\varpi} (\rho^{s} \ddot{\mathbf{u}} \cdot \dot{\mathbf{u}} + \mathcal{F}^{s} \ddot{\boldsymbol{\omega}} \cdot \dot{\boldsymbol{\omega}}) \, dV, \tag{30}$$

$$\mathcal{W}_{abs} = \int_{\mathscr{D}} \int_{\mathscr{B}} \left[ \overline{\mathcal{Z}} \cdot \left( \underline{\dot{U}} - \frac{\dot{\omega}' + \dot{\omega}}{2} \times \underline{Y} \right) + \underline{\mathcal{M}} \cdot (\dot{\omega}' - \dot{\omega}) \right] dV' dV, \quad (31)$$

$$\mathcal{W}_{sup} = \int_{\mathscr{D}} \int_{\mathscr{B} \setminus \mathscr{P}} \left[ \overline{\mathcal{Z}} \cdot \left( \dot{u}' + \frac{\dot{\omega}'}{2} \times \underline{Y}' \right) - \overline{\mathcal{Z}}' \cdot \left( \dot{u} + \frac{\dot{\omega}}{2} \times \underline{Y} \right) \right] dV' dV$$

$$+ \int_{\mathscr{D}} \int_{\mathscr{D} \setminus \mathscr{P}} \left( \underline{\mathcal{M}} \cdot \dot{\omega}' - \underline{\mathcal{M}}' \cdot \dot{\omega} \right) dV' dV + \int_{\mathscr{D}} \left( \rho^{s} \mathbf{g} \cdot \dot{u} + \mathbf{l} \cdot \dot{\omega} \right) dV.$$

(32)

The absorbed energy is equal to the internal energy without considering other sources of energy (e.g., thermal energy) (e.g., Song and Silling, 2020). Thus, it follows from (31) and the assumption of small deformation that the internal energy density can be written as

$$\dot{\mathcal{E}} = \int_{\mathcal{B}} \left[ \overline{\mathcal{T}} \cdot \left( \underline{\dot{U}} - \overline{\underline{\dot{\Omega}}} \times \underline{Y} \right) + \underline{\mathcal{M}} \cdot \underline{\dot{\Omega}} \right] dV' 
= \int_{\mathcal{B}} \left[ \overline{\mathcal{T}} \cdot \left( \underline{\dot{U}} - \overline{\underline{\dot{\Omega}}} \times \underline{X} \right) + \underline{\mathcal{M}} \cdot \underline{\dot{\Omega}} \right] dV' 
= \int_{\mathcal{B}} \left( \overline{\mathcal{T}} \cdot \overline{\underline{\dot{U}}} + \underline{\mathcal{M}} \cdot \underline{\dot{\Omega}} \right) dV' 
= \overline{\mathcal{T}} \cdot \overline{\dot{U}} + \mathcal{M} \cdot \underline{\dot{\Omega}}.$$
(33)

It is implied from (33) that the two peridynamic constitutive relationships can be postulated between the two energy conjugate pairs, respectively, i.e.,  $\overline{\mathcal{T}}$  and  $\underline{\hat{U}}$ , and  $\underline{\mathcal{M}}$  and  $\underline{\Omega}$ . Note that the two constitutive relationships are consistent with the second-law of thermodynamics (e.g., Silling et al., 2007; Song and Silling, 2020), for conciseness whose derivation is omitted here.

In the present study, thermal energy is not considered for simplicity. We refer to the related literature on modeling the shear banding instability of porous media considering fully thermomechanical coupling (e.g., Wang and Song, 2020; Song et al., 2018b). Under the isothermal condition and assuming small elastic strain, the internal energy of the skeleton of a micro-polar elastic porous material can be written as

$$\dot{e} = \overline{\sigma} : \dot{\epsilon} + m : \dot{\kappa}, \tag{34}$$

where  $\overline{\sigma}$  is the effective micro-polar stress tensor,  $\varepsilon$  is the micro-polar strain tensor, m is the couple stress tensor, and  $\kappa$  is the wryness tensor (De Borst and Sluys, 1991; Sulem and Vardoulakis, 1995; Eringen and Eringen, 1999). The micro-polar strain tensor (Eringen and Eringen, 1999) assuming an elastic deformation in the classical Cosserat continuum theory can be written as

$$\varepsilon_{ij} = u_{i,j} - \hat{e}_{kij}\omega_k,$$
(35)

$$\kappa_{ij} = \omega_{i,j},\tag{36}$$

where  $u_i$  is the displacement vector,  $\omega_i$  is the micro-rotation vector,  $\hat{e}_{ijk}$  is the third-order permutation tensor (Malvern, 1969), and i, j, k = 1, 2, 3. Given (35) and (36), the effective micro-polar stress tensor and the couple stress tensor can be computed by the relationships in (63) and (64), respectively, in Section 2.4.1. Following the lines in periporomechanics (Song and Silling, 2020), given  $\underline{\widetilde{U}}$  and  $\underline{\Omega}$  the nonlocal versions of  $\varepsilon$  and  $\kappa$  can be written as

$$\varepsilon = \left[ \int_{\mathscr{L}} \underline{w}(\widetilde{\underline{U}} \otimes \underline{\xi}) dV' \right] \mathscr{K}^{-1}, \tag{37}$$

$$\kappa = \left[ \int_{\mathcal{H}} \underline{w}(\underline{\Omega} \otimes \underline{\xi}) dV' \right] \mathcal{K}^{-1}, \tag{38}$$

where  $\underline{w}$  is a weighting function and  $\mathcal{X}$  is the shape tensor (Silling et al., 2007). The shape function is defined as

$$\mathcal{K} = \int_{\mathscr{L}} \underline{w} \underline{\xi} \otimes \underline{\xi} \, dV'. \tag{39}$$

It follows from (34), (37), and (38) that the rate of the internal energy of a micropolar porous medium can be written as

$$\dot{e} = \int_{\mathcal{H}} \underline{\boldsymbol{\varpi}} \, \overline{\boldsymbol{\sigma}} : (\underline{\widetilde{U}} \otimes \underline{\boldsymbol{\xi}}) \mathcal{K}^{-1} dV' + \int_{\mathcal{H}} \underline{\boldsymbol{\varpi}} \boldsymbol{m} : (\underline{\dot{\Omega}} \otimes \underline{\boldsymbol{\xi}}) \mathcal{K}^{-1} dV' 
= \int_{\mathcal{H}} \left( \underline{\boldsymbol{\varpi}} \, \overline{\boldsymbol{\sigma}} \mathcal{K}^{-1} \underline{\boldsymbol{\xi}} \right) \cdot \underline{\widetilde{U}} dV' + \int_{\mathcal{H}} \left( \underline{\boldsymbol{\varpi}} \boldsymbol{m} \mathcal{K}^{-1} \underline{\boldsymbol{\xi}} \right) \cdot \underline{\dot{\Omega}} dV'.$$
(40)

From the periporomechanics correspondence principle (Song and Silling, 2020), we have

$$\dot{\mathscr{E}} = \dot{e},\tag{41}$$

where  $\mathscr{E}$  is the internal energy density in the Cosserat periporomechanics and its rate form as written in (33). It follows from (41), (33) and (40) that the effective force state and the moment state in Cosserat periporomechanics can be written in terms of the effective stress tensor and moment tensor as

$$\overline{\mathcal{T}} = \underline{w}\overline{\sigma}\mathcal{K}^{-1}\xi,\tag{42}$$

$$\underline{\mathcal{M}} = \underline{w} \mathbf{m} \mathcal{K}^{-1} \xi. \tag{43}$$

From (42) and (43) the Cosserat effective force state and the moment state can be computed from the classical constitutive models given the composite deformation state and micro-rotational state following the lines in classical Cosserat continuum mechanics for solids. In what follows, we first demonstrate the Cosserat periporomechanics correspondence principal suffers from the zero-energy deformation instability mode as in the non-polar periporomechanics. Then we present a stabilization scheme for the Cosserat periporomechanics through which classical micro-polar constitutive models can be incorporated into the Cosserat periporomechanics developed in this article.

#### 2.3. Zero energy modes and stabilization scheme

In this part, we first demonstrate the Cosserat periporomechanics correspondence principal suffers from the zero-energy deformation mode (both translational and micro-rotational) under non-uniform deformation. Then, we present a stabilization scheme to circumvent the zero-energy deformation modes. In what follows, we show the origin of zero-energy deformation modes of the Cosserat periporomechanics correspondence principal. Let us first define the non-uniform composite (micro-polar) displacement state and non-uniform micro-rotation state as follows.

$$\underline{\mathcal{R}}_1 = \underline{\widetilde{U}} - \varepsilon \xi,$$
 (44)

$$\mathcal{R}_{2} = \Omega - \kappa \xi, \tag{45}$$

where  $\epsilon$  and  $\kappa$  are defined in (37) and (38), respectively. Substituting (44) into (37), i.e., by replacing  $\underline{\widetilde{U}}$  by  $\underline{\mathscr{R}}_1$  in (37), we have

$$\begin{split} \left[ \int_{\mathcal{X}} \underline{w}(\underline{\mathcal{R}}_{1} \otimes \underline{\xi}) dV' \right] \mathcal{K}^{-1} &= \left[ \int_{\mathcal{X}} \underline{w}(\underline{\widetilde{U}} - \underline{\mathcal{R}}_{1}\underline{\xi}) \otimes \underline{\xi}) dV' \right] \mathcal{K}^{-1} \\ &= \left[ \int_{\mathcal{X}} \underline{w}(\underline{\widetilde{U}} \otimes \underline{\xi}) dV' \right] \mathcal{K}^{-1} \\ &- \left[ \int_{\mathcal{X}} \underline{w} \varepsilon \underline{\xi} \otimes \underline{\xi} dV' \right] \mathcal{K}^{-1} \\ &= \varepsilon - \varepsilon \mathcal{K} \mathcal{K}^{-1} \\ &= \varepsilon - \varepsilon \end{split}$$

$$= 0. \tag{46}$$

Similarly, substituting (45) into (38) we have

$$\left[\int_{\mathcal{H}} \underline{w}(\underline{\mathcal{R}}_{2} \otimes \underline{\xi}) dV'\right] \mathcal{H}^{-1} = \left[\int_{\mathcal{H}} \underline{w}(\underline{\Omega} - \underline{\mathcal{R}}_{2}\underline{\xi}) \otimes \underline{\xi}) dV'\right] \mathcal{H}^{-1} 
= \left[\int_{\mathcal{H}} \underline{w}(\underline{\Omega} \otimes \underline{\xi}) dV'\right] \mathcal{H}^{-1} 
- \left[\int_{\mathcal{H}} \underline{w} \underline{\kappa}_{\underline{\xi}} \otimes \underline{\xi} dV'\right] \mathcal{H}^{-1} 
= \underline{\kappa} - \underline{\kappa} \mathcal{H} \mathcal{H}^{-1} 
= \underline{\kappa} - \underline{\kappa} 
= 0.$$
(47)

Through (46) and (47) we have demonstrated that the nonuniform micro-polar displacement state and micro-rotational state are smoothed out in the micro-polar periporomechanics correspondence principal. Therefore, the zero-energy deformation mode instability occurs in Cosserat periporomechanics that incorporates the correspondence material models. To resolve this issue, following the lines in Menon and Song (2021b) we develop a stabilization scheme based on an energy method. We refer to Menon and Song (2019) for a comprehensive review of other methods for stabilization schemes of correspondence materials models in the original peridynamics for solids. In this method (Menon and Song, 2021b), the internal energies related to the non-uniform composite displacement state and non-uniform microrotational state are considered in (33). In this case, the total internal energy  $\hat{\mathscr{E}}$  is written as

$$\hat{\mathscr{E}} = \mathscr{E} + \mathscr{E}_{\mathscr{R}_1} + \mathscr{E}_{\mathscr{R}_2}, \tag{48}$$

where  $\mathscr{E}_{\underline{\mathscr{A}}_1}$  and  $\mathscr{E}_{\underline{\mathscr{A}}_2}$  are the energy terms of the non-uniform composite displacement state and non-uniform micro-rotational state, respectively. The two terms are defined as

$$\mathscr{E}_{\underline{\mathscr{R}}_1} = \frac{1}{2} (\underline{\alpha} \underline{\mathscr{R}}_1) \bullet \underline{\mathscr{R}}_1, \tag{49}$$

$$\mathscr{E}_{\underline{\mathscr{R}}_{2}} = \frac{1}{2} (\underline{\beta} \underline{\mathscr{R}}_{2}) \cdot \underline{\mathscr{R}}_{2}, \tag{50}$$

where  $\underline{\alpha}$  and  $\underline{\beta}$  are the two scalar states. Following the lines in Menon and Song (2021b), assuming a micro-polar bond-based periporomechanics the two scalar states can be written as

$$\underline{\alpha} = \frac{\mathcal{G}_1 \mathcal{G}_1}{m_0} \underline{\varpi},$$
(51)

$$\underline{\underline{\rho}} = \frac{\mathcal{G}_2 \mathcal{C}_2}{\varpi_0} \underline{\underline{\varpi}},\tag{52}$$

wher

$$w_0 = \int_{\infty} \underline{\underline{w}} dV',$$
 (53)

and  $\mathscr{G}_1$  and  $\mathscr{G}_2$  are positive constants on the order of 1,  $\mathscr{C}_1$  and  $\mathscr{C}_2$  are two material parameters. For a three-dimensional case, the two parameters can be written as (Menon and Song, 2021b)

$$\mathscr{C}_1 = \frac{12\mathscr{D}}{|\xi|^3},\tag{54}$$

$$\mathscr{C}_2 = \frac{\mathscr{D}}{|\xi|},\tag{55}$$

where  ${\mathcal D}$  is a parameter that depends on the internal length scale (i.e., the horizon and material properties). In the three-dimensional case it reads

$$\mathcal{D} = \frac{E(1 - 4\nu)}{4\pi\delta^2(1 - \nu - 2\nu^2)},\tag{56}$$

where E and v are Young's modulus and Poisson's ratio, respectively. It follows from (49), (50), (42), and (43) the effective force state and moment state with stabilization removing zero energy modes can be written as

$$\underline{\underline{\mathscr{T}}}^{s} = \underline{\underline{w}} \overline{\sigma} \mathscr{K}^{-1} \underline{\xi} + \underline{\alpha} \mathscr{R}_{1}, \tag{57}$$

$$\stackrel{E}{\longleftarrow} \stackrel{\eta}{\square}$$

Fig. 3. Schematic of Maxwell viscoelastic model.

$$\underline{\mathcal{M}}^{s} = \underline{\varpi} \mathbf{m} \mathcal{K}^{-1} \xi + \beta \underline{\mathcal{R}}_{2}. \tag{58}$$

Substituting (57) and (58) the governing equations for Cosserat periporomechanics can be written as

$$\rho^{s} \ddot{\boldsymbol{u}} = \int_{\mathscr{Y}} \left( \overline{\mathscr{Z}}^{s} - \overline{\mathscr{Z}}^{s} \right) dV' + \rho^{s} \boldsymbol{g}, \tag{59}$$

$$\mathcal{J}^{s}\ddot{\boldsymbol{\omega}} = \int_{\mathcal{H}} \left( \underline{\mathcal{M}}^{s} - \underline{\mathcal{M}}^{'s} \right) dV' + \frac{1}{2} \int_{\mathcal{H}} \underline{Y} \times \left( \underline{\overline{\mathcal{T}}}^{s} - \underline{\overline{\mathcal{T}}}^{'s} \right) dV' + I. \tag{60}$$

In what follows, we introduce the classical micro-polar visco-plastic, visco-elastic, and damage models that will be implemented in the proposed Cosserat periporomechanics paradigm.

#### 2.4. Micro-polar rate-dependent constitutive and damage models

We first introduce the classical visco-plastic model and visco-elastic model cast in the framework of the Cosserat continuum theory that take into account the rate-dependency of porous geological materials (Terzaghi et al., 1996). We then present a micro-polar bilinear damage model and an energy damage criterion that incorporates micro-rotation energy.

## 2.4.1. Micro-polar visco-plastic model

The micro-polar visco-plastic model is cast using the Drucker-Prager yield surface. Assuming infinitesimal deformation, the strain tensor  $\epsilon$ and the wryness tensor  $\kappa$  are additively decomposed into elastic and visco-plastic parts as

$$\varepsilon = \varepsilon^e + \varepsilon^{vp},\tag{61}$$

$$\kappa = \kappa^e + \kappa^{vp}. \tag{62}$$

where  $\epsilon^e$  and  $\epsilon^{vp}$  are the elastic and visco-plastic strain tensors, respectively, and  $\kappa^e$  and  $\kappa^{vp}$  are the elastic and visco-plastic wryness tensors, respectively. Given elastic strain and elastic wryness tensors, the effective stress tensor  $\overline{\sigma}$  and couple stress tensor m can be expressed

$$\overline{\sigma} = \lambda t r(\varepsilon^e) 1 + (\mu + \mu_e) \varepsilon^e + (\mu - \mu_e) \varepsilon^{e^T}, \tag{63}$$

$$\mathbf{m} = \alpha_1 t \mathbf{r}(\kappa^e) 1 + \alpha_2 \kappa^e + \alpha_3 \kappa^{e^T}, \tag{64}$$

where  $\lambda$  and  $\mu$  are Láme's first elastic constant and elastic shear modulus, respectively, which can be determined from Young's modulus and Poisson's ratio (Malvern, 1969), the superscript T is the transpose operator, and  $\mu_c$ ,  $\alpha_1$ ,  $\alpha_2$  and  $\alpha_3$  are the micro-polar parameters (Gauthier and Jahsman, 1975; de Borst, 1993; Eringen and Eringen, 1999).

The stress tensor and couple stress tensor can be written in a vector form as form

$$\tilde{\boldsymbol{\sigma}} = \{\overline{\sigma}_{11}, \overline{\sigma}_{22}, \overline{\sigma}_{33}, \overline{\sigma}_{12}, \overline{\sigma}_{21}, \overline{\sigma}_{13}, \overline{\sigma}_{31}, \overline{\sigma}_{23}, \overline{\sigma}_{32}\}^T$$

$$(65)$$

$$\tilde{\mathbf{m}} = \{m_{11}/l, m_{22}/l, m_{33}/l, m_{12}/l, m_{21}/l, m_{13}/l, m_{31}/l, m_{23}/l, m_{32}/l\}^{T},$$
 (66)

where l is the Cosserat length scale (de Borst, 1993). In this study, only one Cosserat length scale is assumed. We refer to Sulem and Vardoulakis (1995) for more discussions on Cosserat length scales. It follows from (65) and (66) that the mean stress  $\bar{p}$  and the deviatoric stress q (Mühlhaus and Vardoulakis, 1987; de Borst, 1993) can be written as

$$\bar{p} = (\tilde{\sigma}_1 + \tilde{\sigma}_2 + \tilde{\sigma}_3)/3, \tag{67}$$

$$q = \left[\frac{1}{2} (\tilde{\boldsymbol{\sigma}}^T \tilde{\mathbb{P}} \tilde{\boldsymbol{\sigma}} + \tilde{\boldsymbol{m}}^T \tilde{\tilde{\mathbb{P}}} \tilde{\boldsymbol{m}})\right]^{\frac{1}{2}}.$$
 (68)

$$\tilde{\mathbb{P}} = \begin{bmatrix} 2 & -1 & -1 \\ -1 & 2 & -1 \\ -1 & -1 & 2 \\ & & 3/2 & 3/2 \\ & & & 3/2 & 3/2 \\ & & & & 3/2 & 3/2 \\ & & & & & 3/2 & 3/2 \\ & & & & & & 3/2 & 3/2 \\ & & & & & & & 3/2 & 3/2 \\ & & & & & & & & 3/2 & 3/2 \\ & & & & & & & & 3/2 & 3/2 \\ & & & & & & & & & 3/2 & 3/2 \\ & & & & & & & & & & 3/2 & 3/2 \\ & & & & & & & & & & & & & & \end{bmatrix},$$
 (69)

and

$$\tilde{\mathbb{P}} = 3I_{9\times 9},\tag{70}$$

where  $I_{9\times9}$  is the 9-dimensional second-order identity matrix (i.e.,  $\delta_{ij}$ with i, j = 1, ..., 9). Given  $\bar{p}$  and q, the Cosserat Drucker-Prager yield function (Li and Tang, 2005) is written as

$$f = q + \sqrt{3} \mathcal{A}_1 \overline{p} + \mathcal{A}_2. \tag{71}$$

$$\mathcal{A}_1 = \frac{2\sin\varphi}{\sqrt{3}(3-\sin\varphi)},$$

$$\mathcal{A}_2 = \frac{-6c\cos\varphi}{\sqrt{3}(3-\sin\varphi)},$$
(72)

$$\mathcal{A}_2 = \frac{-6c\cos\varphi}{\sqrt{3}(3-\sin\varphi)},\tag{73}$$

where  $\varphi$  is the frictional angle. Here, we adopt a linear isotopic hardening as

$$c = c_0 + h\hat{\varepsilon}^p. \tag{74}$$

where  $c_0$  is the initial cohesion, h is the linear isotropic hardening modulus, and  $\hat{\epsilon}^p$  is a visco-plastic internal variable, as defined in (79). Assuming the non-associative plasticity, the plastic flow potential (De Borst and Sluys, 1991; Li and Tang, 2005) can be defined as

$$g = q + \sqrt{3}\mathcal{A}_3\overline{p} + \mathcal{A}_2,\tag{75}$$

$$\mathcal{A}_3 = \frac{2\sin\psi}{\sqrt{3}(3-\sin(\psi))},\tag{76}$$

and  $\psi$  is the dilatancy angle.

Given (75), the visco-plastic strain and wryness tensors can be determined as

$$\dot{e}^{vp} = \frac{\langle f \rangle}{\eta} \frac{\partial g}{\partial \bar{\sigma}},\tag{77}$$

$$\dot{\varepsilon}^{\nu p} = \frac{\langle f \rangle}{\eta} \frac{\partial g}{\partial \overline{\sigma}},\tag{77}$$

$$\dot{\kappa}^{\nu p} = \frac{\langle f \rangle}{\eta} \frac{\partial g}{\partial m},\tag{78}$$

where  $\eta$  is the viscosity of the skeleton and  $\langle \ \rangle$  is the Macaulay bracket (Malvern, 1969), i.e., a ramp function defined as  $\langle x \rangle = \frac{x + |x|}{2}$ . The internal viscoplastic variable can be defined as

$$\dot{\hat{\epsilon}}^p = \left(\frac{1}{3}\dot{\epsilon}_s^{vp} : \dot{\epsilon}_s^{vp} + \frac{1}{3}\dot{\epsilon}_s^{vp} : \dot{\epsilon}_s^{vp,T} + \frac{2}{3}\dot{\kappa}^{vp} : \dot{\kappa}^{vp}\right)^{1/2},\tag{79}$$

where  $\varepsilon_s^{vp}$  is the deviatoric part of the visco-plastic strain tensor. By substituting (77) and (78) into (79) the internal visco-plastic variable can be written as

$$\dot{\hat{\varepsilon}}^p = \frac{\langle f \rangle}{\eta} \left[ 1 + \operatorname{sign}(\bar{p}) \frac{\mathcal{A}_3}{\sqrt{3}} \right]. \tag{80}$$

# 2.4.2. Micro-polar visco-elastic model

In this subsection, we introduce the micro-polar visco-elastic model (Lakes and Lakes, 2009) for the simulations of cracking in Section 4. The strain and wryness tensors are additively decomposed into elastic and visco-elastic parts as

$$\varepsilon = \varepsilon^e + \varepsilon^{ve},\tag{81}$$

$$\kappa = \kappa^e + \kappa^{ve}. \tag{82}$$

where  $\epsilon^{ve}$  and  $\kappa^{ve}$  are visco-elastic strain and wryness tensors, respectively. Given the elastic strain and wryness tensors, (63) and (64) can be used to compute the stress and couple stress for the micropolar viscoelastic model.

Following the simple Maxwell model as shown in Fig. 3, the evolution equation for the micro-polar visco-elastic model (Marques and Creus, 2012) can be written as

$$\dot{\boldsymbol{\epsilon}}^{ve} + \frac{\boldsymbol{\epsilon}^{ve}}{\tau} = \dot{\boldsymbol{\epsilon}},\tag{83}$$

$$\dot{\mathbf{k}}^{ve} + \frac{\mathbf{k}^{ve}}{\tau_r} = \dot{\mathbf{k}},\tag{84}$$

where  $\tau_r$  is the relaxation time.

It follows from (83), (84), (63), and (64), the stress and couple stress in the integral form (Marques and Creus, 2012) can be written as

$$\sigma = \int_0^t \exp\left(\left[(\tau - t)/\tau_r\right]\right) \left[\lambda \frac{dtr(\epsilon)1}{d\tau} + (\mu + \mu_e) \frac{d\epsilon}{d\tau} + (\mu - \mu_e) \frac{d\epsilon^T}{d\tau}\right] d\tau,$$
(85)

$$\mathbf{m} = \int_0^t \exp\left[(\tau - t)/\tau_r\right] \left[ \alpha_1 \frac{dt r(\kappa)1}{d\tau} + \alpha_2 \frac{d\kappa}{d\tau} + \alpha_3 \frac{d\kappa^T}{d\tau} \right] d\tau.$$
 (86)

For the micro-polar visco-elastic correspondence model, the effective force and moment states (Silling et al., 2007) can be written as

$$\overline{\underline{\mathscr{T}}} = \underline{\overline{t}} \left( \frac{\underline{\widetilde{U}}}{|\underline{\widetilde{U}}|} \right), \tag{87}$$

$$\underline{\mathcal{M}} = \underline{m} \left( \frac{\underline{\Omega}}{|\underline{\Omega}|} \right), \tag{88}$$

where  $\bar{t}$  and m are the scalar effective force and moment states, respectively, and  $\underline{U}_{\bar{\Omega}}/|\underline{U}_{\bar{\Omega}}|$  and  $\underline{\Omega}/|\underline{\Omega}|$  denote the directions of the effective force and moment vector states, respectively. For a bond-based visco-elastic micropolar material model, the effective force state can be decomposed into the part parallel to the bond  $\bar{t}_1$  and the part perpendicular to the bond  $\bar{t}_2$  as

$$\bar{\underline{t}}_{1} = \frac{1}{2} f_{1}(\underline{u}_{1}), \tag{89}$$

$$\underline{\overline{t}}_2 = \frac{1}{2} f_2(\boldsymbol{u}_2, \boldsymbol{\omega}),\tag{90}$$

where  $u_1$  and  $u_2$  are the displacements in the axial and the normal directions of the bond, respectively. Fig. 4 presents a schematic of the decomposition of deformation states and force states for the micro-polar visco-elasticity model.

For a bond-based micro-polar visco-elastic model, the bond stretch rate  $\dot{s}_1$  and the shear deformation rate  $\dot{s}_2$  (Yu and Chen, 2021) can be defined as

$$\dot{s}_1 = \frac{|\Delta \dot{u}_1|}{|\xi|},\tag{91}$$

$$\dot{s}_2 = \frac{|\Delta \dot{u}_2 - \frac{\dot{\Omega}}{\underline{\zeta}}\underline{\xi}|}{|\underline{\xi}|}.$$
 (92)

Fig. 5 sketches the concept for a special case of the visco-elastic material model. We note that a summary of the pairwise deformation mechanisms of the model can be found in Diana and Casolo (2019).

Following the linear micro-polar elasticity, it is assumed that the total bond stretch  $s_1$ , shear deformation  $s_2$ , and the relative micro rotation  $\Delta\omega$  (magnitude) can be decomposed into elastic and visco-elastic parts as

$$s_1 = s_1^e + s_1^{ve} (93)$$

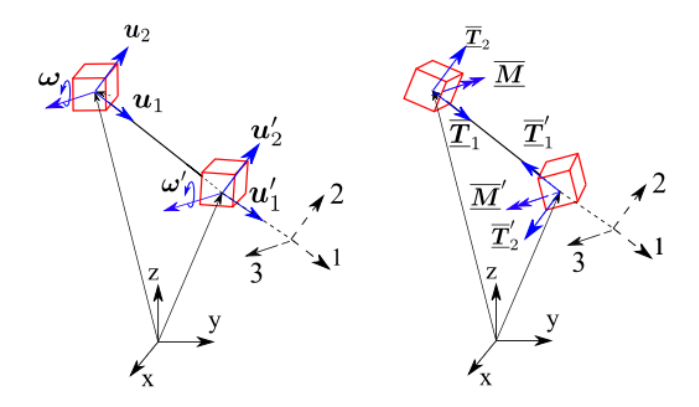


Fig. 4. Schematic of the decomposition of deformation states and force states for the micro-polar visco-elasticity model.

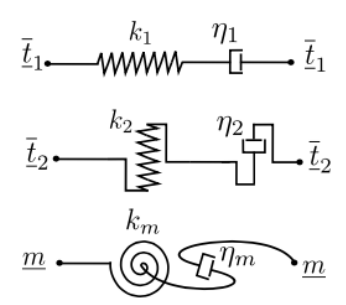


Fig. 5. Schematic of a simple viscoelastic micropolar model.

$$s_2 = s_2^e + s_2^{ve}, (94)$$

$$\Delta \omega = \Delta \omega^e + \Delta \omega^{ve}. \tag{95}$$

where  $s_1^e$  and  $s_1^{ve}$  are elastic and visco-elastic stretches, respectively,  $s_2^e$ and  $s_2^{ve}$  are elastic and visco-elastic shear deformations, respectively, and  $\Delta \omega^e$  and  $\Delta \omega^{ve}$  are the elastic and visco-elastic relative rotations (magnitude), respectively. The scalar axial and normal force and scalar moment states can be defined as

$$\underline{\bar{t}}_1 = k_1 s_1^e, \tag{96}$$

$$\bar{t}_2 = k_2 s_2^e, \tag{97}$$

$$m = k_m \Delta \omega^e, \tag{98}$$

where  $k_1$ ,  $k_2$ , and  $k_m$  are the material constants. They can be determined from the elastic modulus and the horizon (Chen et al., 2019; Gerstle et al., 2007) as

$$k_1 = \frac{3E}{2\pi\delta^4(1-2\nu)} \frac{1}{|\xi|},\tag{99}$$

$$k_{1} = \frac{3E}{2\pi\delta^{4}(1-2\nu)} \frac{3E}{|\xi|},$$

$$k_{2} = \frac{E(1-4\nu)}{\pi\delta^{2}(1-\nu-2\nu^{2})} \frac{3}{|\xi|^{3}},$$

$$k_{m} = \frac{E(1-4\nu)}{4\pi\delta^{2}(1-\nu-2\nu^{2})} \frac{1}{|\xi|}.$$
(100)

$$k_m = \frac{E(1-4\nu)}{4\pi\delta^2 (1-\nu-2\nu^2)} \frac{1}{|\xi|}.$$
 (101)

The evolution equations for the bond-based micro-polar visco-elastic model can be written as

$$\dot{s}^{ve} + \frac{s^{ve}}{\tau_1} = \dot{s},\tag{102}$$

$$\dot{s}_{2}^{ve} + \frac{s_{2}^{ve}}{2} = \dot{s}_{2},\tag{103}$$

$$\Delta \dot{\omega}^{ve} + \frac{\Delta \omega^{ve}}{\tau_m} = \Delta \dot{\omega}. \tag{104}$$

where  $\tau_1$ ,  $\tau_2$  and  $\tau_m$  are the relaxation time for the axial force, normal force, and moment, respectively. For simplicity, in this study it is

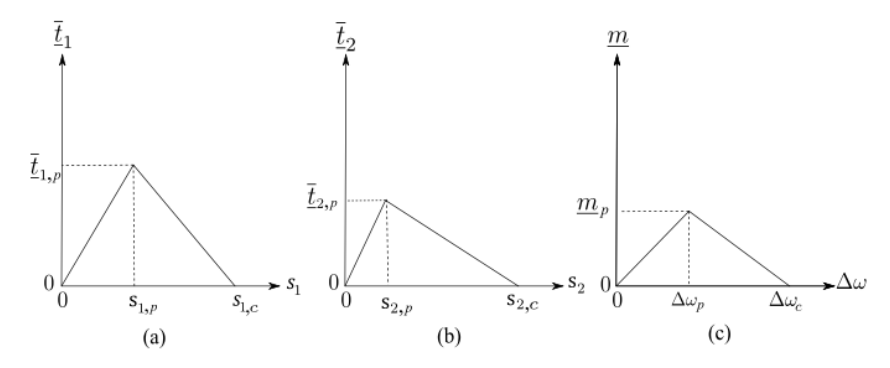


Fig. 6. Schematic of the bilinear micro-polar damage model: (a) axial force, (b) normal force, and (c) moment.

assumed that  $\tau_1 = \tau_2 = \tau_m = \tau_r$ . This constitutive model in the integration form can be written as

$$\underline{\bar{t}}_1 = \int_0^t k_1 \exp\left[(\tau - t)/\tau_r\right] \frac{ds_1}{d\tau} d\tau, \tag{105}$$

$$\underline{\bar{t}}_2 = \int_0^t k_2 \exp\left[(\tau - t)/\tau_r\right] \frac{ds_2}{d\tau} d\tau, \tag{106}$$

$$\underline{m} = \int_0^t k_m \exp\left[(\tau - t)/\tau_r\right] \frac{d\Delta\omega}{d\tau} d\tau. \tag{107}$$

In what follows, we introduce a bilinear micro-polar damage model.

#### 2.4.3. Ordinary micro-polar damage model

In this study, we present an ordinary micro-polar bilinear damage model (Silling et al., 2010) for modeling the softening behavior of quasi brittle porous media. Fig. 6 presents a schematic of the bilinear micro-polar damage model

It follows from Fig. 6 that the micro-polar bilinear damage model

$$\underline{\bar{l}}_{1} = \begin{cases}
k_{1}s_{1}^{e} & \text{if } s_{1} \leq s_{1,p}, \\
(s_{1,c} - s_{1})/(s_{1,c} - s_{1,p})\underline{\bar{l}}_{1,p} & \text{if } s_{1,p} < s_{1} < s_{1,c}, \\
0 & \text{if } s_{1} \geqslant s_{1,c},
\end{cases}$$
(108)

$$\underline{\overline{t}}_{2} = \begin{cases}
k_{2}s_{2}^{e} & \text{if } s_{1} \geq s_{2,p}, \\
(s_{2,c} - s_{2})/(s_{2,c} - s_{2,p})\underline{\overline{t}}_{2,p} & \text{if } s_{2,p} < s_{2} < s_{2,c}, \\
0 & \text{if } s_{2} \geq s_{2,c},
\end{cases}$$

$$\underline{m} = \begin{cases}
k_{m}\Delta\omega^{e} & \text{if } \Delta\omega \leq \Delta\omega_{p}, \\
(\Delta\omega_{c} - \Delta\omega)/(\Delta\omega_{c} - \Delta\omega_{p})\underline{m}_{p} & \text{if } \Delta\omega_{p}^{e} < \Delta\omega < \Delta\omega_{c}, \\
0 & \text{if } \Delta\omega \geq \Delta\omega_{c},
\end{cases}$$
(110)

$$\underline{m} = \begin{cases} k_m \Delta \omega^e & \text{if } \Delta \omega \leqslant \Delta \omega_p, \\ (\Delta \omega_c - \Delta \omega) / (\Delta \omega_c - \Delta \omega_p) \underline{m}_p & \text{if } \Delta \omega_p^e < \Delta \omega < \Delta \omega_c, \\ 0 & \text{if } \Delta \omega \geqslant \Delta \omega_c, \end{cases}$$
(110)

where  $s_{1,p},\ s_{2,p},$  and  $\Delta\omega_p$  are the axial and shear deformation and the relative rotation corresponding to the peak values of  $\underline{t}_1$ ,  $\underline{t}_2$ , and  $\underline{m}$ , respectively, and  $s_{1,c}$ ,  $s_{2,c}$ , and  $\Delta\omega_c$  are the critical values of  $s_1$ ,  $s_2$ , and  $\Delta\omega$ , respectively. These material parameters can be determined and calibrated by comparing numerical results with experimental testing data for given materials.

In this study, it is assumed that the bond breakage for the bondbased micro-polar model is determined by the axial stretch for its simplicity. In this case, the weighting function  $\varpi$  for the bond can be

$$\underline{\underline{\sigma}} = \begin{cases} 1 & \text{if } s_1 \leqslant s_{1,p}, \\ \frac{s_{1,c} - s_1}{s_{1,c} - s_{1,p}} & \text{if } s_{1,p} < s_1 < s_{1,c}, \\ 0 & \text{if } s_1 \ge s_{1,c}. \end{cases}$$
(111)

Given w, the local damage parameter at a material point (Silling and Askari, 2005) can be defined as

$$D = 1 - \frac{\int_{\mathcal{H}} \underline{\varpi} dV'}{\int_{\mathcal{H}} dV'}.$$
 (112)

#### 2.4.4. Energy-based bond breakage criterion

In this study, we also formulate an energy-based criterion to detect the bond breakage for the micro-polar visco-elastic correspondence material model. We note that an energy-based criterion for the bondbased micro-polar model accounting for the axial, shear and eventually micro-bending can be found in Diana (2023). The energy-based bond breakage criterion will be used for detecting the crack propagation in example 4 in Section 4. In this case, the bond-breakage criterion depends on the deformation energy in a bond. The effective force state and the moment state (the energy conjugates of the composite state and relative rotation state, respectively) are used to determine the deformation energy (Menon and Song, 2022d). Therefore, the energy density in bond  $\xi$  can be written as

$$W = \int_{0}^{t} (\overline{Z} - \overline{Z}') \underline{\widetilde{U}} dt + \int_{0}^{t_{f}} (\underline{M} - \underline{M}') \underline{\dot{\Omega}} dt.$$
 (113)

where t is the loading time. In this case, the weighting function for a bond  $\xi$  can be defined as

$$\underline{\underline{w}} = \begin{cases} 1 & \text{if } \mathcal{W} < \mathcal{W}_{cr}, \\ 0 & \text{if } \mathcal{W} \ge \mathcal{W}_{cr}. \end{cases}$$
 (114)

Given (114), the local damage parameter at a material point can be expressed by (112).

It is noted that the critical energy density for bond breakage can be calculated from the critical energy release rate as

$$W_{cr} = \frac{4\mathcal{G}_{cr}}{\pi\delta^4}. (115)$$

In the linear elastic fracture mechanics for mode I fracture the critical energy release rate reads

$$\mathcal{G}_{cr} = \mathcal{K}_I^2 \frac{1 - v^2}{E},\tag{116}$$

where  $K_I$  is the fracture toughness of mode I crack. In this study, it is assumed that the crack propagation (including branching) is due to individual bond breakage at the crack tip. The mode I fracturing energy is adopted for the correspondence micro-polar material model for its simplicity. For mode II and mode III cracks, the corresponding fracture toughness can be used following the linear elastic fracture mechanics. It follows from (114) that the local damage parameter at a material point can be determined from (112).

The field equations of CPPM in this study are formulated based on the peridynamic states in which the fundamental unknowns are displacement and micro-rotation of each material point. The classical micro-polar material model for the solid skeleton is used to compute the effective force state and moment state in the field equations through the Cosserat periporomechanics correspondence principle. Therefore, the formulation in this study can be used to compute a field, such as displacement and micro-rotation, in a problem domain. In the following section, we present the numerical implementation of the proposed Cosserat periporomechanics paradigm for deformable porous media under dry conditions.

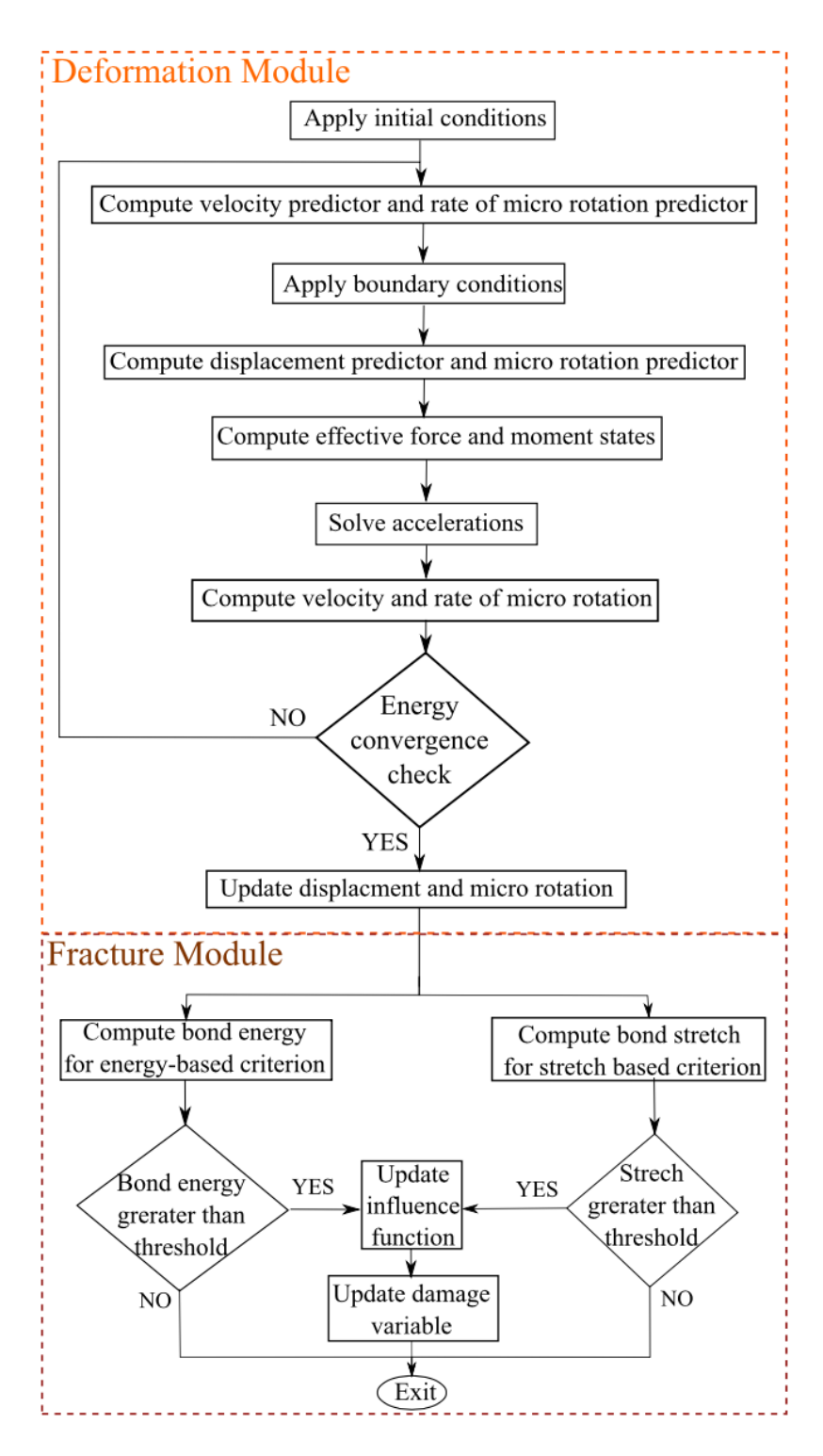


Fig. 7. Global flowchart for the computational Cosserat PPM paradigm for dry porous media.

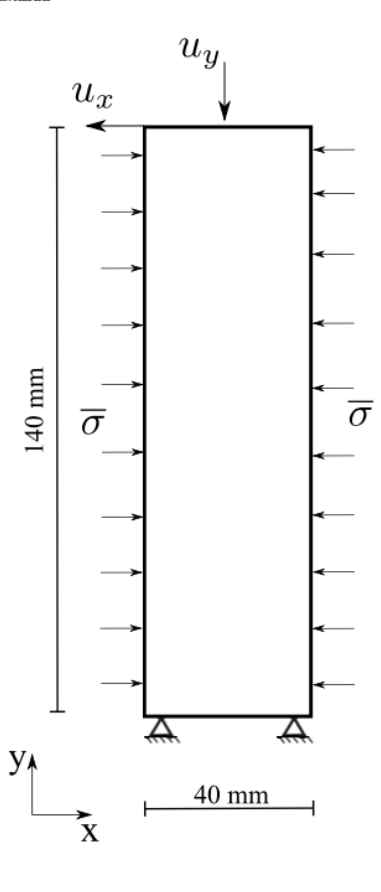


Fig. 8. Problem setup for example 1.

# 3. Numerical implementation

We have numerically implemented the proposed Cosserat periporomechanics paradigm through an explicit Lagrangian meshfree scheme (Menon and Song, 2022c). Fig. 7 presents a schematic of the global flowchart of the numerical implementation. The energy conservation criterion (Belytschko et al., 2014) is adopted to guarantee the convergence at each time step. In what follows, we first present the spatial discretization, followed by the temporal discretization of the governing equations.

# 3.1. Discretization in space

The motion equation (59) and the moment equation (60) are discretized in space by the total Lagrangian meshfree scheme (Menon and Song, 2021b, 2022a,c). In this method, a porous continuum material is discretized into a finite number of mixed material points (i.e., solid skeleton and pore water). Under the dry condition, each material point has two kinds of degrees of freedom (i.e., displacement and microrotation). The uniform grid is used to spatially discretize the problem domain in which all material points have the same dimensions. The spatial discretization forms of (59) and (60) are written as

$$\mathbf{0} = \mathcal{A}_{i-1}^{\mathcal{P}}(\overline{\mathcal{M}}_{i}\ddot{\mathbf{u}}_{i} - \overline{\mathcal{T}}_{i} + \mathcal{F}_{i}), \tag{117}$$

$$\mathbf{0} = \mathcal{A}_{i=1}^{P}(\mathcal{F}_{i}\ddot{\boldsymbol{\omega}}_{i} - \mathcal{M}_{i} + \widetilde{\mathcal{M}}_{i} + \mathcal{L}_{i}), \tag{118}$$

where  $\mathscr{A}$  is a global linear assembly operator (Menon and Song, 2021a; Hughes, 2012),  $\overline{\mathscr{M}}_i$  is the mass matrix at material point i,  $\overline{\mathscr{T}}_i$  is the vector of effective force,  $\mathscr{F}_i$  is the vector gravity force (Menon and Song, 2022c),  $\mathscr{M}_i$  is the vector of rotational moment,  $\widetilde{\mathscr{M}}_i$  is the moment by the

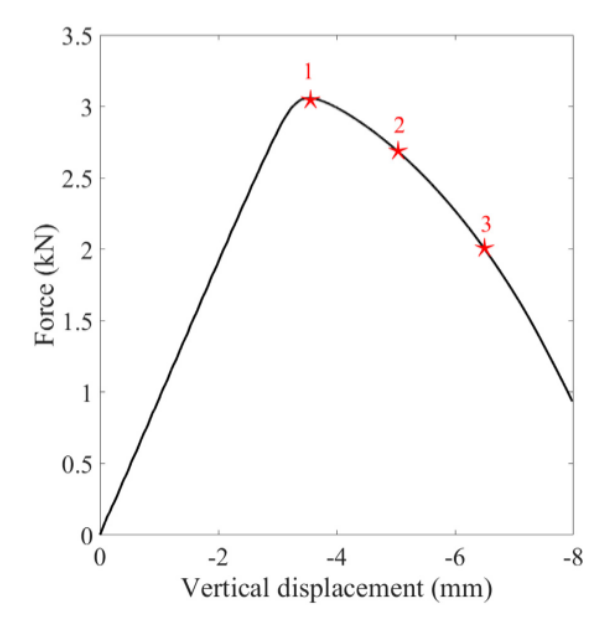


**Fig. 9.** Loading curve on the top boundary. Note: The displacements at points 1, 2, 3 are  $u_{y,1} = 3.5$  mm,  $u_{y,2} = 5$  mm and  $u_{y,3} = 6.5$  mm, respectively.

effective force state, and  $\mathcal{L}_i$  is the body couple vector. At material point i, these five vectors through the stabilized correspondence material model can be written as

$$\overline{\mathcal{M}}_i = \rho_s \phi_i \mathcal{V}_i \mathbf{1},\tag{119}$$

$$\overline{\mathcal{T}}_{i} = \sum_{i=1}^{\mathcal{N}_{i}} \left( \underline{\overline{\mathcal{T}}}_{(ij)}^{s} - \underline{\overline{\mathcal{T}}}_{(ji)}^{s} \right) \mathcal{V}_{j} \mathcal{V}_{i}, \tag{120}$$

$$\mathcal{I}_i = \mathcal{I}_i \mathcal{V}_i \mathbf{1},$$
 (121)

$$\mathcal{M}_{i} = \sum_{i=1}^{\mathcal{N}_{i}} \left( \underline{\mathcal{M}}_{(ij)}^{s} - \underline{\mathcal{M}}_{(ji)}^{s} \right) \mathcal{V}_{j} \mathcal{V}_{i}, \tag{122}$$

$$\widetilde{\mathcal{M}}_{i} = \sum_{i=1}^{\mathcal{N}_{i}} \left[ \frac{1}{2} \underline{Y}_{(ij)} \left( \underline{\mathcal{Z}}_{(ij)}^{s} - \underline{\mathcal{Z}}_{(ji)}^{s} \right) \right] \mathcal{V}_{j} \mathcal{V}_{i}, \tag{123}$$

where  $\mathcal{V}_i$  and  $\mathcal{V}_j$  are the volumes of material points i and j, respectively, in the reference configuration. In (120), (122) and (123), the effective force state and the moment state through the stabilized correspondence principle are written as

$$\overline{\underline{\mathcal{T}}}_{(ij)}^{s} = \underline{\omega}_{(ij)} \overline{\boldsymbol{\sigma}}_{(i)} \mathcal{K}_{(i)}^{-1} \underline{\boldsymbol{\xi}}_{(ij)} + \underline{\alpha} \underline{\mathcal{R}}_{1(ij)}, \tag{124}$$

$$\overline{\underline{\mathcal{T}}}_{(ji)}^{s} = \underline{\omega}_{(ji)} \overline{\sigma}_{(j)} \mathcal{K}_{(j)}^{-1} \underline{\xi}_{(ji)} + \underline{\alpha} \underline{\mathcal{R}}_{1(ji)}, \tag{125}$$

$$\underline{\mathcal{M}}_{(ij)}^{s} = \underline{\boldsymbol{\varpi}}_{(ij)} \boldsymbol{m}_{(i)} \mathcal{K}_{(i)}^{-1} \underline{\boldsymbol{\xi}}_{(ij)} + \underline{\boldsymbol{\mu}} \underline{\mathcal{R}}_{2(ij)}, \tag{126}$$

$$\underline{\mathcal{M}}_{(ji)}^{s} = \underline{w}_{(ji)} \mathbf{m}_{(j)} \mathcal{K}_{(j)}^{-1} \underline{\xi}_{(ji)} + \underline{\beta} \underline{\mathcal{R}}_{2(ji)}. \tag{127}$$

The micro-polar strain tensor and the wryness tensor can be written as

$$\boldsymbol{\varepsilon}_{(i)} = \left[ \sum_{j=1}^{\mathcal{N}_i} \underline{\boldsymbol{\varpi}}_{(ij)} (\underline{\widetilde{\boldsymbol{U}}}_{(ij)} \otimes \underline{\boldsymbol{\xi}}_{(ij)}) \mathcal{V}_j \right] \mathcal{X}_{(i)}^{-1}, \tag{128}$$

$$\boldsymbol{\kappa}_{(i)} = \left[ \sum_{j=1}^{\mathcal{N}_i} \underline{\boldsymbol{w}}_{(ij)} (\underline{\Omega}_{(ij)} \otimes \underline{\boldsymbol{\xi}}_{(ij)}) \mathcal{V}_j \right] \mathcal{K}_{(i)}^{-1}. \tag{129}$$

Given  $\varepsilon_{(i)}$  and  $\kappa_{(i)}$ , classical constitutive models can be used to compute  $\overline{\sigma}_{(i)}$  and  $m_{(i)}$  as described in Section 2.4. In what follows we present the discretization in time through an explicit Newmark scheme (Zienkiewicz et al., 1999; Hughes, 2012).

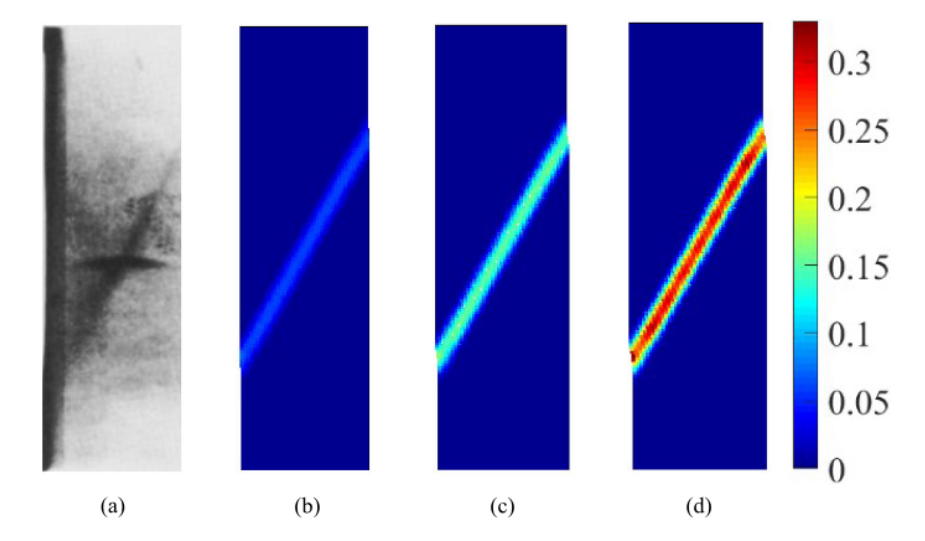


Fig. 10. (a) Shear band in the experimental test (Mühlhaus and Vardoulakis, 1987) and the contours of the equivalent plastic shear strain at the three loading stages: (b)  $u_{y,1} = 3.5$  mm, (c)  $u_{y,2} = 5$  mm, and (d)  $u_{y,3} = 6.5$  mm.

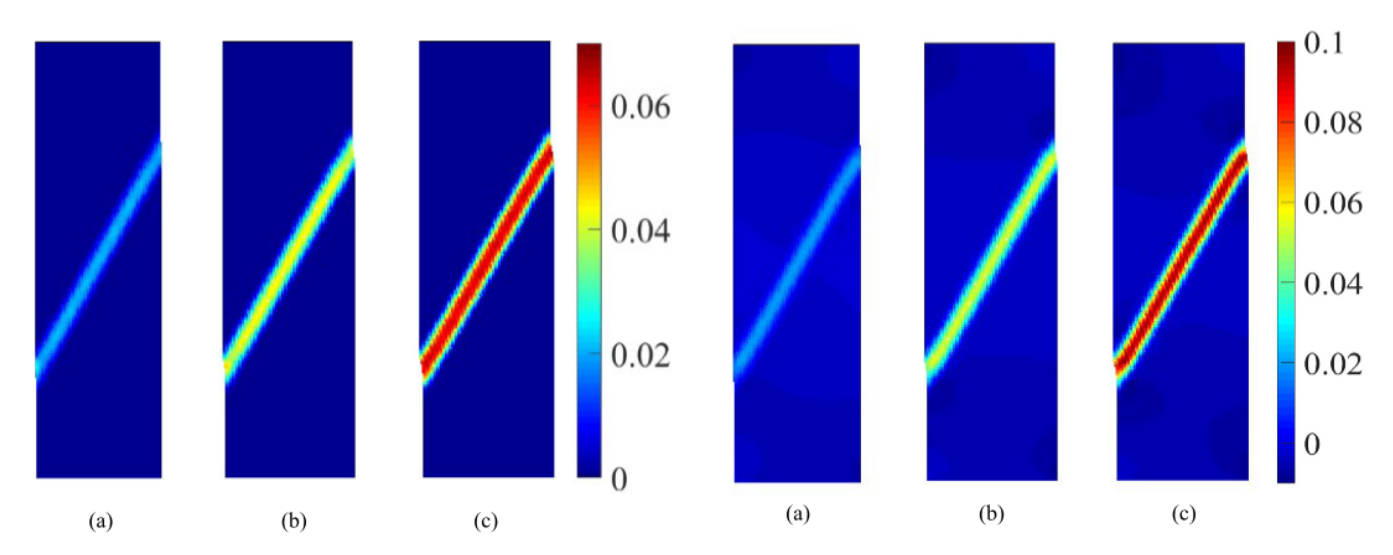


Fig. 11. Contours of the plastic volumetric strain at three loading stages: (a)  $u_{y,1}=3.5$  mm, (b)  $u_{y,2}=5$  mm, and (c)  $u_{y,3}=6.5$  mm.

Fig. 12. Contours of the micro rotation (rad) at three loading stages: (a)  $u_{y,1}=3.5$  mm, (b)  $u_{y,2}=5$  mm, and (c)  $u_{y,3}=6.5$  mm.

#### 3.2. Discretization in time

The Newmark scheme (Hughes, 2012) is applied to integrate the equations of motion and moment in time. Let  $u_n$ ,  $\dot{u}_n$  and  $\ddot{u}_n$  be the displacement, velocity, and acceleration vectors at time step n. The predictors of displacement and velocity in a general Newmark scheme read

$$\widetilde{\boldsymbol{u}}_{n+1} = \dot{\boldsymbol{u}}_n + (1 - \beta_1) \Delta \ddot{\boldsymbol{u}}_n, \tag{130}$$

$$\widetilde{\boldsymbol{u}}_{n+1} = \boldsymbol{u}_n + \Delta t \dot{\boldsymbol{u}}_n + \frac{\Delta t^2}{2} \left( 1 - 2\beta_2 \right) \ddot{\boldsymbol{u}}_n, \tag{131}$$

$$\dot{\widetilde{\boldsymbol{\omega}}}_{n+1} = \dot{\boldsymbol{\omega}}_n + (1 - \beta_1) \Delta \ddot{\boldsymbol{\omega}}_n, \tag{132}$$

$$\widetilde{\boldsymbol{\omega}}_{n+1} = \boldsymbol{\omega}_n + \Delta t \dot{\boldsymbol{\omega}}_n + \frac{\Delta t^2}{2} \left( 1 - 2\beta_2 \right) \dot{\boldsymbol{\omega}}_n, \tag{133}$$

where  $\beta_2$  and  $\beta_1$  are numerical integration parameters. Given (130) and (131), the accelerations  $\ddot{u}_{n+1}$  and  $\omega$  are determined by the recursion relation

$$\ddot{u}_{n+1} = \overline{\mathcal{M}}_{n+1}^{-1}(\mathcal{F}_{n+1} - \widetilde{\overline{\mathcal{F}}}_{n+1}), \tag{134}$$

$$\ddot{\omega}_{n+1} = \mathcal{I}_{n+1}^{-1}(\mathcal{L}_{n+1} - \widetilde{M}_{n+1} + \widetilde{\widetilde{M}}_{n+1}), \tag{135}$$

where  $\widetilde{\overline{\mathcal{T}}}_{n+1}$ ,  $\widetilde{\mathcal{M}}_{n+1}$ , and  $\widetilde{\mathcal{M}}_{n+1}$  are determined from (131) and (133) and the local constitutive models. From (134) and (135), the displacement, velocity, rotation, and rotation rate at time step n+1 can be updated as

$$\dot{\boldsymbol{u}}_{n+1} = \widetilde{\boldsymbol{u}}_{n+1} + \beta_1 \Delta t \ddot{\boldsymbol{u}}_{n+1},\tag{136}$$

$$u_{n+1} = \widetilde{u}_{n+1} + \beta_2 \Delta t^2 \ddot{u}_{n+1}. \tag{137}$$

$$\dot{\boldsymbol{\omega}}_{n+1} = \widetilde{\boldsymbol{\omega}}_{n+1} + \beta_1 \Delta t \ddot{\boldsymbol{\omega}}_{n+1},\tag{138}$$

$$\boldsymbol{\omega}_{n+1} = \widetilde{\boldsymbol{\omega}}_{n+1} + \beta_2 \Delta t^2 \ddot{\boldsymbol{\omega}}_{n+1}. \tag{139}$$

In this study, we adopt the explicit central difference solution scheme (Hughes, 2012; Zienkiewicz et al., 1999) in which  $\beta_1=1/2$  and  $\beta_2=0$ . We note that the explicit method is efficient and robust to model dynamic problems (Silling and Askari, 2005).

The energy balance check is used to ensure numerical stability of the algorithm in time (Belytschko et al., 2014). We define the internal energy, external energy, and kinetic energy of the system at time step

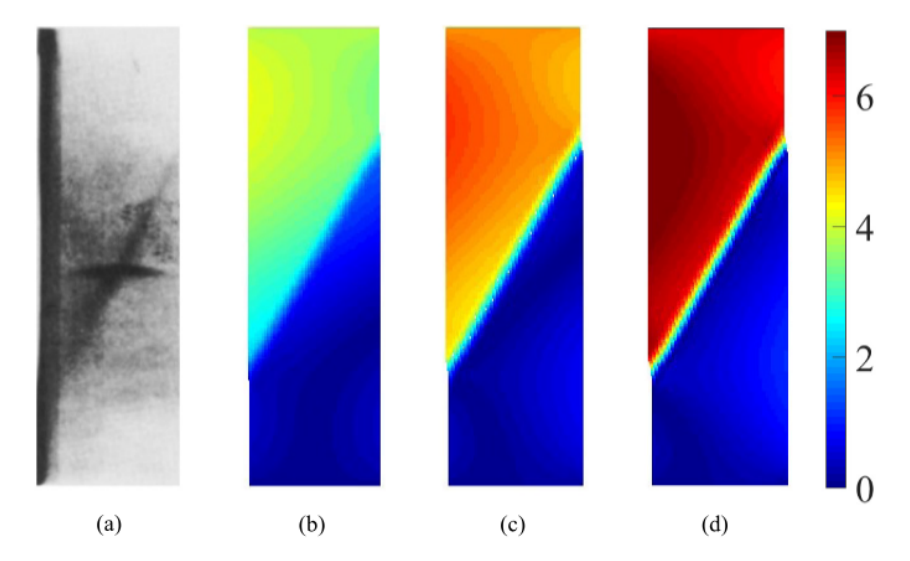


Fig. 13. (a) Shear band in the experimental test (Mühlhaus and Vardoulakis, 1987) and the contours of the displacement magnitude (mm) at three loading stages: (b)  $u_{y,1} = 3.5$  mm, (c)  $u_{y,2} = 5$  mm and (d)  $u_{y,3} = 6.5$  mm.

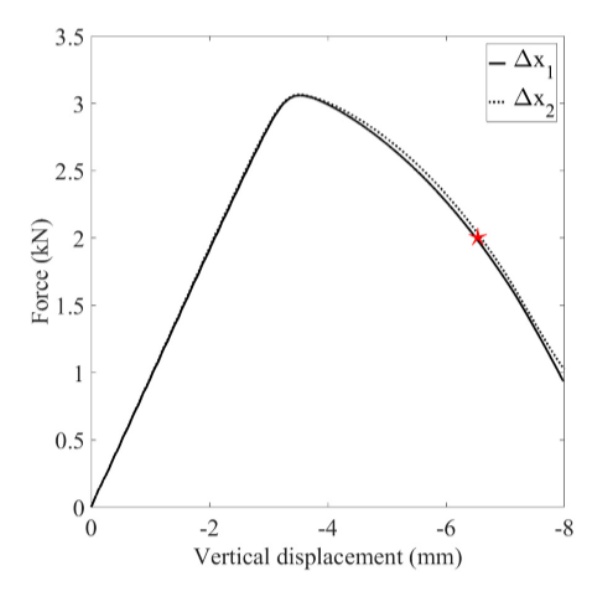


Fig. 14. Comparison of the vertical loading curves from the simulations with two spatial discretization schemes.

n+1 as

$$\mathcal{W}_{\text{int},n+1} = \mathcal{W}_{\text{int},n} + \frac{\Delta t}{2} \left( \dot{\boldsymbol{u}}_{n} + \frac{\Delta t}{2} \ddot{\boldsymbol{u}}_{n} \right) \left( \overline{\mathcal{F}}_{n} + \overline{\mathcal{F}}_{n+1} \right) \\
+ \frac{\Delta t}{2} \left( \dot{\boldsymbol{o}}_{n} + \frac{\Delta t}{2} \ddot{\boldsymbol{o}}_{n} \right) \left[ \left( \mathcal{M}_{n} - \widetilde{\mathcal{M}}_{n} \right) \right. \\
+ \left( \mathcal{M}_{n+1} - \widetilde{\mathcal{M}}_{n+1} \right) \right], \tag{140}$$

$$\mathcal{W}_{\text{ext},n+1} = \mathcal{W}_{\text{ext},n} + \frac{\Delta t}{2} \left( \dot{\boldsymbol{u}}_{n} + \frac{\Delta t}{2} \ddot{\boldsymbol{u}}_{n} \right) \left( \mathcal{F}_{n} + \mathcal{F}_{n+1} \right)$$

$$+\frac{\Delta t}{2}\left(\dot{\boldsymbol{\omega}}_{n}+\frac{\Delta t}{2}\ddot{\boldsymbol{\omega}}_{n}\right)\left(\boldsymbol{\mathcal{L}}_{n}+\boldsymbol{\mathcal{L}}_{n+1}\right),\tag{141}$$

$$\mathcal{W}_{\text{kin},n+1} = \frac{1}{2} \dot{\boldsymbol{u}}_{n+1} \overline{\mathcal{M}}_{n+1} \dot{\boldsymbol{u}}_{n+1} + \frac{1}{2} \dot{\boldsymbol{o}}_{n+1} \mathcal{I}_{n+1} \dot{\boldsymbol{o}}_{n+1}. \tag{142}$$

Then it follows from the energy conservation criterion that

$$|\mathcal{W}_{\text{int},n+1} + \mathcal{W}_{\text{kin},n+1} - \mathcal{W}_{\text{ext},n+1}| \leq \hat{\varepsilon} \max \left( \mathcal{W}_{\text{int},n+1}, \mathcal{W}_{\text{kin},n+1}, \mathcal{W}_{\text{ext},n+1} \right), \tag{143}$$

where  $\hat{\epsilon}$  is a small tolerance on the order of  $10^{-2}$  (Belytschko et al., 2014).

For the numerical implementation algorithms for the micro-polar visco-plastic and visco-elastic models, we refer to the related literature on the subject (e.g., de Borst (1993), De Borst (1991), Simo and Hughes (1998)). Algorithm 1 summarizes the detailed steps in the explicit numerical scheme.

#### 4. Numerical examples

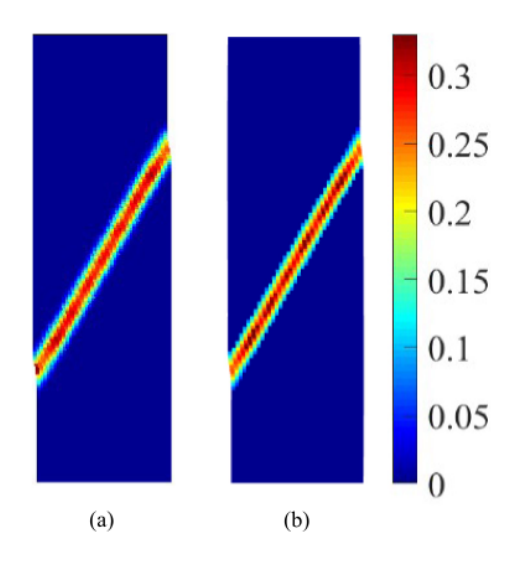
This section presents four numerical examples to validate and demonstrate the efficacy and robustness of the proposed Cosserat periporomechanics model in simulating the shear banding and fracturing in porous media. Example 1 deals with the single shear banding in a sand specimen. Example 2 concerns the cracking of a quasi-brittle porous medium under a three-point bending test. Example 3 deals with the conjugate shear banding under the dynamic loading condition. Example 4 concerns crack branching in porous media under high loading rates. In all examples, the boundary conditions (i.e., essential and natural boundary conditions) are prescribed through the fictitious boundary layer method (Silling, 2000; Menon and Song, 2021a). For all examples in this section, the material points on the boundary layers are free to have micro-rotations. In this study, the horizon — the nonlocal length scale is assumed to be correlated to the Cosserat length scale. The latter is related to the particle micro-rotation. In this sense, the nonlocal length scale in CPPM has a physical meaning related to the materials' microstructure (Sulem and Vardoulakis, 1995).

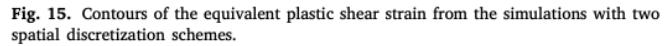
# 4.1. Example 1: Single shear banding

This example simulates a single shear banding in granular materials under non-symmetrical loading conditions. The numerical results are compared with the experimental testing of shear banding of granular materials in Sulem and Vardoulakis (1995). Fig. 8 shows the specimen dimensions, boundary conditions, and the loads. The constant confining pressure is 0.196 MPa. The total vertical displacement imposed on the top boundary is  $u_y=8$  mm. The lateral displacement  $u_x=1.6$  mm is applied on the top boundary to induce the single shear band in the specimen. The rates of the two displacement loads are  $\dot{u}_y=0.2$  m/s and  $\dot{u}_x=0.04$  m/s, respectively. As in Sulem and Vardoulakis (1995), the input material parameters are: the density  $\rho^s=1650$  kg/m³, shear modulus  $\mu=50.4$  MPa, Poisson's ratio  $\nu=0.1$ , Cosserat shear modulus  $\mu_c=2$   $\mu$ , initial volume fraction  $\phi_0=0.65$ , and Cosserat length scale

# Algorithm 1 Explicit Newmark time integration scheme

```
Given: \vec{u}_n, \dot{\vec{u}}_n, \vec{\omega}_n, \dot{\vec{\omega}}_n, D_n, t_n, \Delta t. Compute: \vec{u}_{n+1}, \dot{\vec{u}}_{n+1}, \ddot{\vec{u}}_{n+1}, \ddot{\vec{\omega}}_{n+1}, \dot{\vec{\omega}}_{n+1}, \ddot{\vec{\omega}}_{n+1}, D_{n+1}
 1: Update time t_{n+1} = t_n + \Delta t
 2: while t_{n+1} \le t_f do
          Compute \tilde{\vec{u}}_{n+1} and \tilde{\vec{\omega}}_{n+1} using (130) and (132), respectively
 3:
 4:
          Update boundary conditions at t_{n+1}
          Compute \vec{u}_{n+1} and \vec{\omega}_{n+1} using (131) and (133), respectively
 5:
          Compute \overline{\mathcal{T}}_{n+1}, \widetilde{\mathcal{M}}_{n+1}, and \widetilde{\mathcal{M}}_{n+1} using (120), (122), and (123), respectively
 6:
 7:
          Compute M_{n+1} and \mathcal{F}_{n+1}
          Compute \ddot{\vec{u}}_{n+1} and \ddot{\vec{\omega}}_{n+1} using (134) and (135), respectively
 8:
 9:
          Update \vec{u}_{n+1} and \vec{\omega}_{n+1} using (136) and (138), respectively
          Compute W_{kin,n+1}, W_{int,n+1}, and W_{ext,n+1} using (142), (140), and (141), respectively
10:
          Check energy balance
11:
           Update \vec{u}_{n+1} and \vec{\omega}_{n+1} using (137) and (139), respectively
12:
          for all points do
13:
14:
               for each neighbor do
                    Compute W for energy-based bond breakage criterion
15:
16:
                    Compute s_1, s_2 and \Delta \omega for stretch-based bond breakage criterion
17:
                    Update <u>w</u>
                    Update D_{n+1}
18:
19:
                end for
           end for
20:
21: end while
22: n \leftarrow n + 1
```





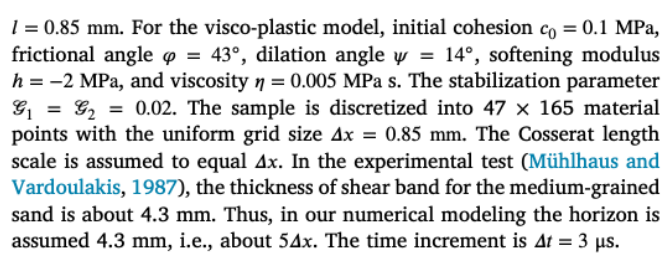


Fig. 9 plots the loading curve on the top boundary, which shows a softening stage following the peak load. The three points on the loading curve are selected to demonstrate the shear band formation in what follows. Figs. 10, 11, 12 and 13 present the snapshots of equivalent plastic shear strain, plastic volumetric strain, micro-rotation and the displacement magnitude at the three loading stages, respectively. The

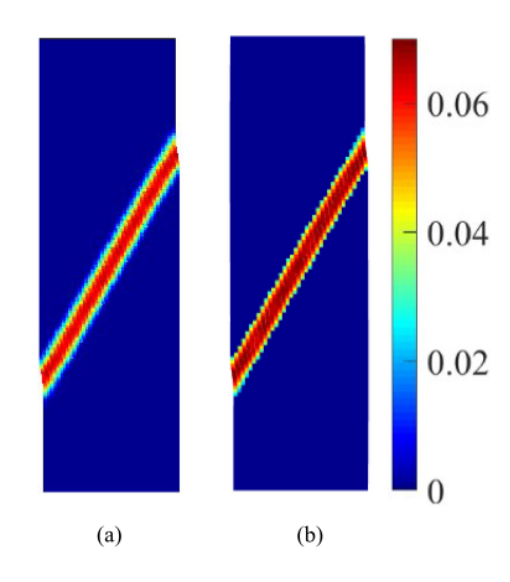


Fig. 16. Contours of the plastic volume strain from the simulations with two spatial discretization schemes.

results in Figs. 10 and 13 show that the shear band develops gradually with an inclination angle of 60° with respect to the *x*-direction. The inclination angle of the shear band is close to the biaxial test results, i.e., 59°, as in Sulem and Vardoulakis (1995), Vardoulakis and Graf (1985). Fig. 11 shows that the plastic volumetric strain is positive within the shear band, which is typical for a medium-dense granular material. Fig. 12 plots the contour of the micro-rotation at the three loading stages. The results show the micro-rotation mainly occurs with the material points within the shear band (Sulem and Vardoulakis, 1995). It is noted that the shear band thickness of the numerical simulation is 4.3 mm which agrees well with the experimental testing result (Mühlhaus and Vardoulakis, 1987). Fig. 13 compares the contours of the displacement magnitude with the experimental results that demonstrates our numerical simulation can replicate the shear banding observed in the laboratory testing.

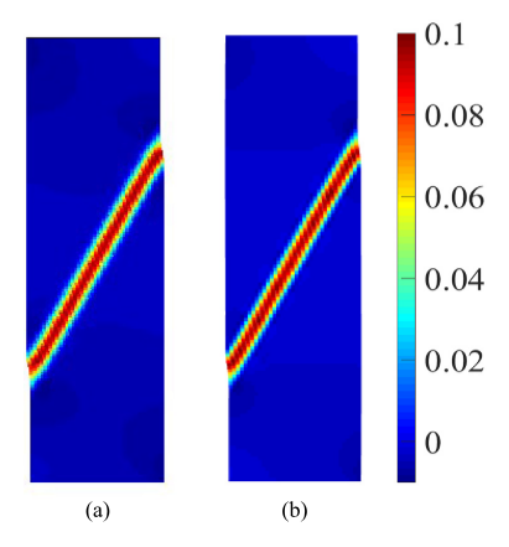


Fig. 17. Contours of the micro rotation (rad) from the simulations with two spatial discretization schemes.

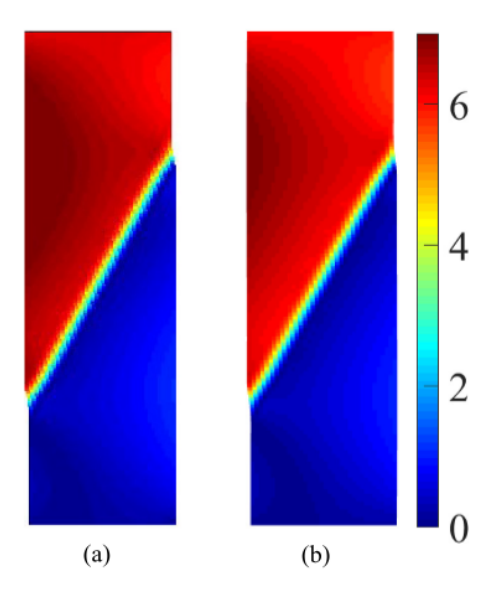


Fig. 18. Contours of the displacement magnitude (mm) from the simulations with two spatial discretization schemes.

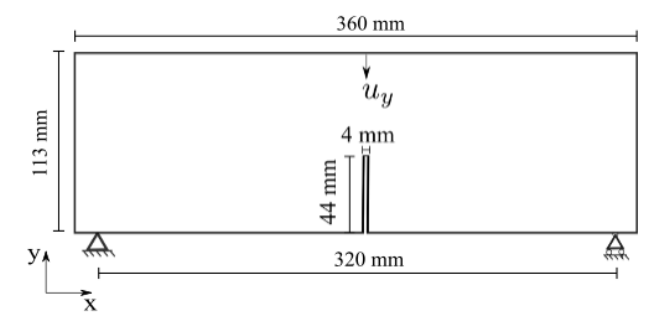


Fig. 19. Model setup for example 2.

Next, we study the influence of spatial discretizations on the results. We consider two spatial discretization schemes, i.e.,  $47 \times 165$  points with  $\Delta x = 0.85$  mm and  $37 \times 130$  points with  $\Delta x = 1.07$  mm. The same horizon  $\delta = 4.3$  mm is assumed for the two cases. The others input

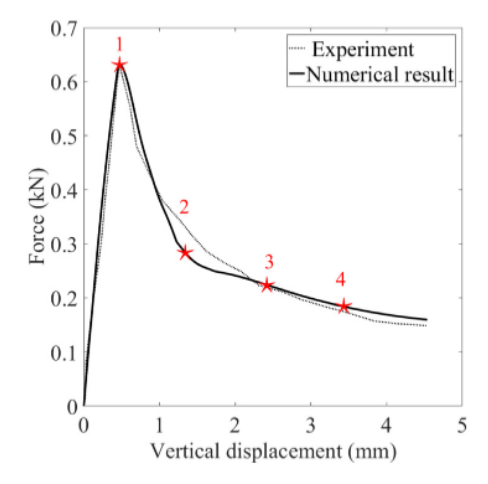


Fig. 20. Comparison of loading curves of the numerical result and the experimental

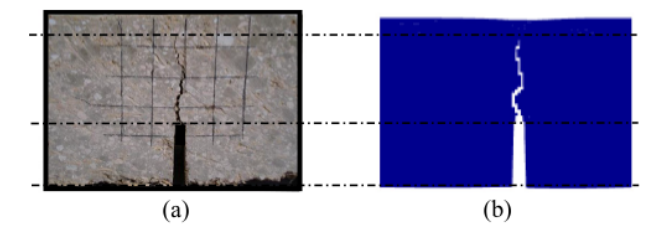


Fig. 21. (a) Crack path from the experimental test (Lenci et al., 2012) and (b) crack path from the numerical model.

parameters remain the same. Fig. 14 shows the loading curves of the two simulations. The loading curves are exactly the same before the peak load and are lightly different after the peak load. Figs. 15, 16, 17 and 18 compare the contours of the equivalent plastic shear strain, plastic volumetric strain, micro rotation, and displacement magnitude at  $u_y = 6.5$  mm, respectively. The results in Figs. 15–18 demonstrate that the numerical results is insensitive to the spatial discretization scheme due to the same horizon assumed for the two simulations.

#### 4.2. Example 2: Cracking in a three-point bending test

This example simulates crack propagation in a quasi-brittle porous material under the three-point bending test (Lenci et al., 2012). Fig. 19 shows the model setup for this example. The specimen is discretized into 10314 uniform material points with  $\Delta x = 2$  mm. The horizon size is chosen as  $\delta = 3.015 \ \Delta x$ . The vertical displacement load  $u_v = 5 \ \mathrm{mm}$  is imposed at the center of the top boundary under the rate  $\dot{u}_v = 3.55 \text{ m/s}$ . The time increment is  $\Delta t = 2 \,\mu s$ . The bilinear visco-elastic damage model is adopted in this example. The material parameters (Lenci et al., 2012) are: solid density  $\rho^s = 2500 \text{ kg/m}^3$ , initial volume fraction  $\phi_0 =$ 0.85, Young's modulus E = 350 MPa, Poisson's ratio v = 0.3. We assume that Cosserat shear modulus  $\mu_c = \mu/3$ , relaxation time  $\tau_r = 8 \times 10^3 \, \mu s$ , and Cosserat length scale is l=2 mm. The damage parameters for the axial bond stretch are assumed as  $s_{1,p}=0.004$  and  $s_{1,c}=0.225$ . It is further assumed that the bilinear damage model for the shear force and moment follows the bilinear damage model for the axial force in terms of the timing of peak and null values at the critical shear deformation and micro-rotation.

Fig. 20 plots the loading curve of the experimental test and the numerical simulation in this study. The results in Fig. 20 show that the numerical result agrees well with the experimental data. Our numerical model can reasonably predict the softening regime in the loading curve.

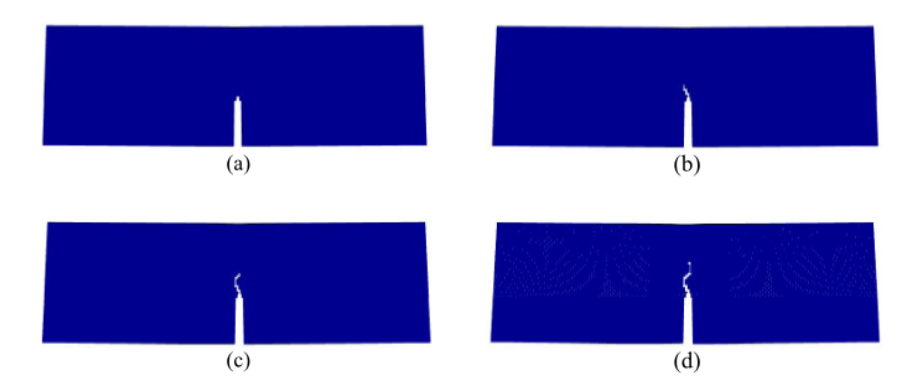


Fig. 22. Crack propagation in the deformed configurations at (a)  $u_{y,1} = 0.5$  mm, (b)  $u_{y,2} = 1.5$  mm, (c)  $u_{y,3} = 2.5$  mm, and (d)  $u_{y,4} = 3.5$  mm.

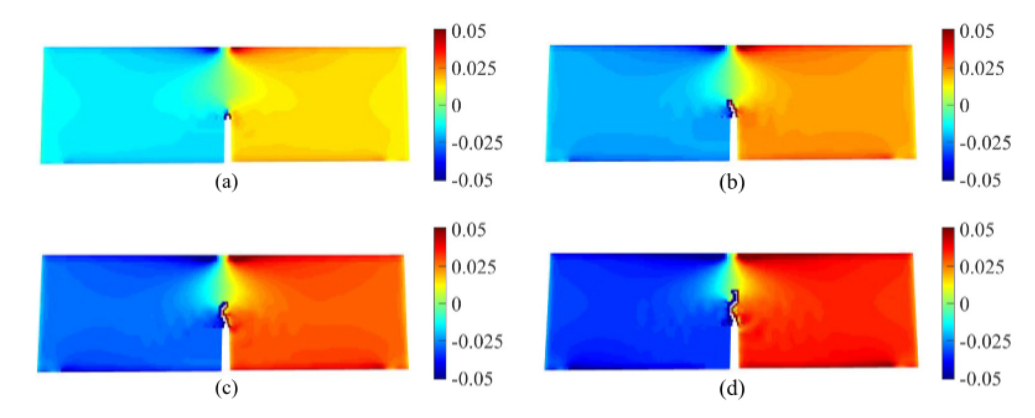


Fig. 23. Contours of micro-rotation (rad) in the deformed configurations at (a)  $u_{y,1} = 0.5$  mm, (b)  $u_{y,2} = 1.5$  mm, (c)  $u_{y,3} = 2.5$  mm, and (d)  $u_{y,4} = 3.5$  mm.

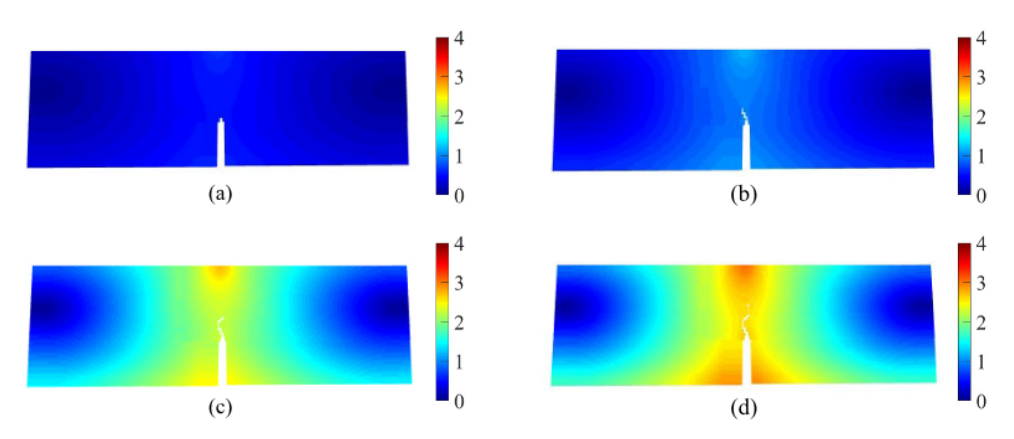


Fig. 24. Contours of the displacement magnitude (mm) in the deformed configurations at (a)  $u_{y,1} = 0.5$  mm, (b)  $u_{y,2} = 1.5$  mm, (c)  $u_{y,3} = 2.5$  mm, and (d)  $u_{y,4} = 3.5$  mm.

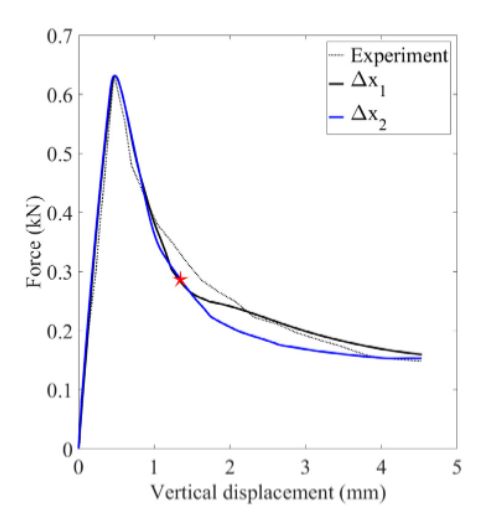


Fig. 25. Comparison of the loading curves from the numerical simulations with two spatial discretization schemes and the experimental data.

Fig. 21 compares the crack path from the numerical model with the experimental data. As shown in Fig. 21, the crack path predicted by the numerical model is consistent with the experimental data. Next, the results at the four loading stages shown in Fig. 20 are presented to show the crack propagation under loading. Figs. 22 and 23 plot the contours of crack path and micro-rotation in the deformed configurations at the four loading stages, respectively. Fig. 22 shows that the crack propagates upward tortuously. Fig. 23 shows that the material points with micro-rotations are concentrated on the crack tip. The magnitude of micro-rotation increases as the crack propagates upward. Finally, Fig. 24 plots the contours of the displacement magnitude at the four displacements.

In what follows, we present the results of the simulations with two spatial discretization schemes with the same horizon  $\delta=6$  mm. For the two cases, the specimen is discretized into 10314 uniform points ( $\Delta x_1=2$  mm) and 4584 uniform points ( $\Delta x_2=3$  mm), respectively. Fig. 25 compares the loading curves of the two simulations with the experimental result. The point corresponding to  $u_y=1.5$  mm is marked in Fig. 25. The two loading curves from the numerical modeling are consist and a slight discrepancy occurs at a later loading stage after the peak load. Figs. 26 and 27 plot the crack propagation and the contours of micro-rotation in the deformed configuration at  $u_y=1.5$  mm, respectively. Fig. 28 compares the contour of displacement in the deformed configuration at  $u_y=1.5$  mm. The results in Figs. 27–28 demonstrate that with the same horizon the numerical results are less influenced by spatial discretization schemes.

#### 4.3. Example 3: Conjugate shear banding

This example deals with the conjugate shear banding in viscoplastic porous media under dry conditions. We investigate the impact of the dilation angle on the directions of the two conjugate shear bands in the specimen under symmetrical loading conditions. Fig. 29 plot the model setup for this example.

The specimen is discretized into  $40 \times 80$  material points with a uniform grid size  $\Delta x = 2.5$  mm and the horizon size  $\delta = 2.05$   $\Delta x$ . The lateral confining pressure of 0.1 MPa is applied on the left and right boundaries. A vertical displacement is applied on the top and bottom boundaries  $u_y = 4.5$  mm with the rate  $\dot{u}_y = 0.05$  m/s. The simulation time  $t = 1 \times 10^4$  µs with a stable time increment  $\Delta t = 7$  µs. The stabilization parameters  $\mathcal{G}_1 = 0.01$  and  $\mathcal{G}_2 = 0.001$  are used for stabilization in the pre-localization and post-localization stages, respectively.

Table 1
Comparison of the inclination angles (°) from the close-form solution and the numerical results.

φ(°)	Ψ(°)	Roscoe solution	Numerical solution
35	0	45	41.3
35	10	50	46.6
35	20	55	50.9

The micro-polar visco-plastic material model is adopted for this example. The input material parameters are as follows. The density  $\rho^s = 2000 \text{ kg/m}^3$ , Young's modulus E = 50 MPa, Poisson's ratio v = 0.2, Cosserat shear modulus  $\mu_c = 2$   $\mu$ , initial volume fraction  $\phi_0 = 0.65$ , and Cosserat length scale l = 2 mm. The viscoplastic parameters are initial cohesion  $c_0 = 0.5$  MPa, softening modulus h = -1 MPa, and viscosity  $\eta = 0.01$  MPa s.

First, we investigate the influence of the dilatation angle on the inclination angle of the shear band. We consider three dilatation angles = 0°, 10°, and 20° assuming the same frictional angle  $\varphi = 35^{\circ}$ . Fig. 30 plots the loading curves from the simulations with the three dilation angles. Fig. 30 shows that the loading curves are the same until the peak load. In the post-localization regime, the dilatation angle has little influence on the loading curve. At the same last load step, the simulation with the null dilation angle generates the smallest reaction force. Figs. 31 and 32 plot the contours of equivalent plastic shear strain and plastic volumetric strain from the simulations with three dilation angles at the same last load step, respectively. Fig. 33 plots the micro rotation contours on the deformed configurations from the three simulations at the same end load step. The results in Figs. 31, 32, and 33 demonstrate that the dilation angle affects the inclination of the two conjugate shear bands. Fig. 33 shows that the micro rotation of material points is localized within the shear band.

Table 1 compares the inclination angle of the shear band in this example with the classical Roscoe solution. Our numerical solution is consistent with the Roscoe solution (Sulem and Vardoulakis, 1995). The second-order work is useful to detect shear bands in porous media (Kakogiannou et al., 2016; Hill, 1958; Menon and Song, 2022e). Therefore, the second-order work criterion is used to validate our numerical results. The second-order work dW for a micropolar PPM material can be written as

$$d\mathcal{W} = d\overline{\sigma} : d\varepsilon + d\mathbf{m} : d\kappa. \tag{144}$$

Fig. 34 plots the contours of the second-order work from the three dilation angles. The results show that the second-order work within the shear band is negative for all three cases.

Second, we study the influence of loading rates on the formation of shear bands with three loading rates,  $\dot{u}_{y,1} = 0.083$  m/s,  $\dot{u}_{y,2} = 0.067$  m/s and  $\dot{u}_{v,3} = 0.05$  m/s. The frictional angle  $\varphi = 35^{\circ}$  and the dilatation angle  $\psi = 15^{\circ}$ . The other material parameters remain the same. Fig. 35 presents the loading curves from the three loading rates. It shows that the loading rate mainly affects the peak and post-localization regimes. Figs. 36, 37, and 38 present the contours of equivalent plastic shear strain, micro rotation, and plastic volume strain at the same final loading stage, respectively. The results show that the loading rate affects the width of shear bands, e.g., decreasing loading rates decreases the width of shear bands. This loading rate impact on the shear-band width is due to the visco-plastic constitutive model adopted in this study. For a rate-independent porous media, it can be conjectured that the shearband width is independent of the loading rate. Furthermore, Fig. 39 demonstrates that the zone of negative second-order work is consistent with the location of shear bands. We note that the second-order work is computed at each material points through (144). Following the secondorder work criterion the second-order work become zero or negative when a material loses its stability. Thus, in the post-localization stage, the second-order work in the shear band become negative. In this example, the negative second-order work in the shear band demonstrates the

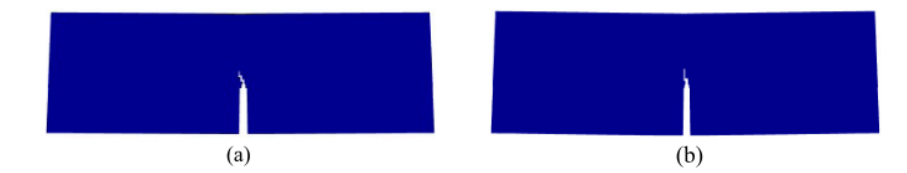


Fig. 26. Crack propagation at  $u_y = 1.5$  mm from the simulations with two spatial discretization schemes: (a)  $\Delta x = 2$  mm and (b)  $\Delta x = 3$  mm.

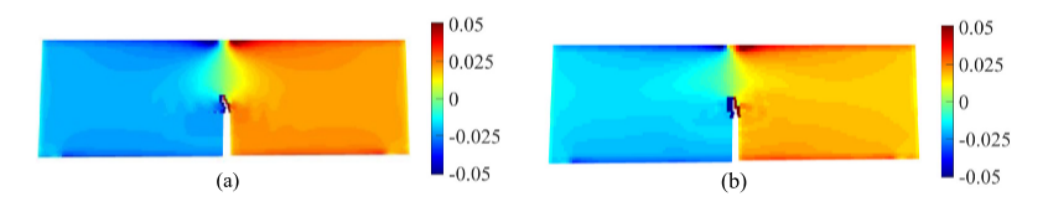


Fig. 27. Contours of the micro rotation (rad) in the deformed configurations at  $u_y = 1.5$  mm from the simulations with two spatial discretization schemes: (a)  $\Delta x = 2$  mm and (b)  $\Delta x = 3$  mm.

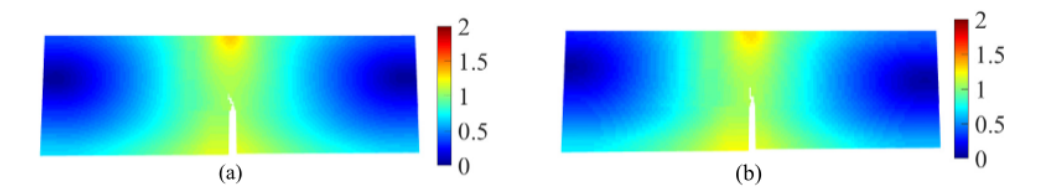
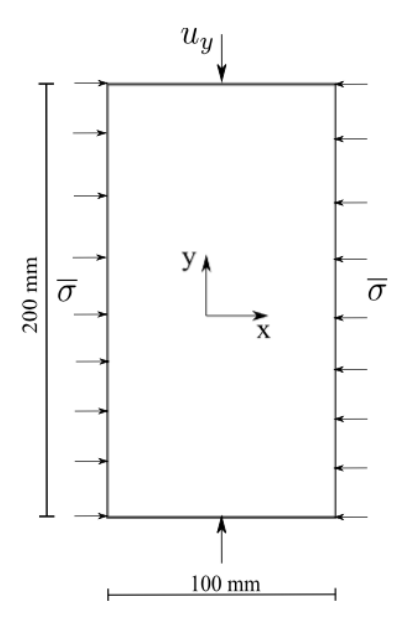
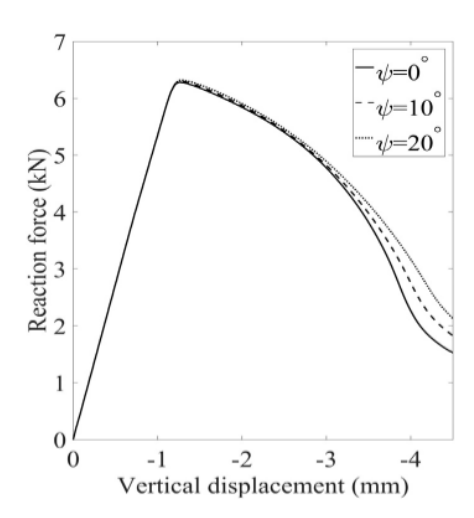


Fig. 28. Contours of the displacement magnitude (mm) in the deformed configurations at  $u_y = 1.5$  mm from the simulations with two spatial discretization schemes: (a)  $\Delta x = 2$  mm and (b)  $\Delta x = 3$  mm.



 $\textbf{Fig. 29.} \ \ \textbf{Geometry, boundary conditions, and the loading of the conjugate shear banding.}$ 



**Fig. 30.** Loading curves assuming three dilatation angles  $\psi=0^\circ$ ,  $\psi=10^\circ$ , and  $\psi=20^\circ$  (the same frictional angle  $\varphi=35^\circ$ ).

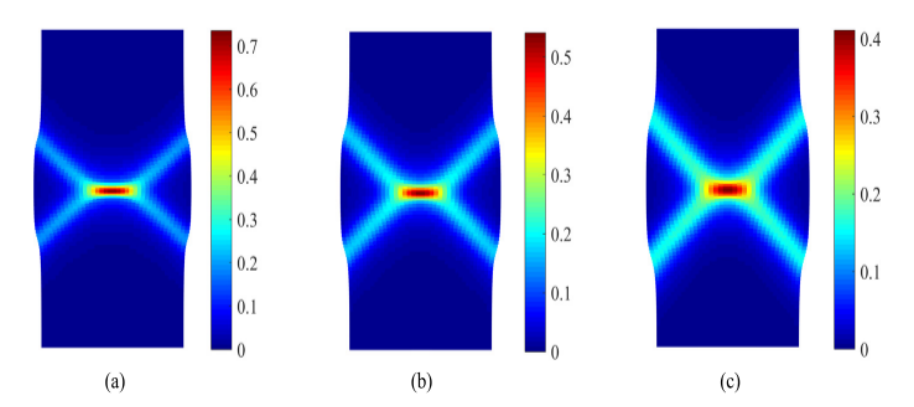


Fig. 31. Contours of the plastic shear strain assuming three dilatation angles: (a)  $\psi = 0^{\circ}$  (inclination angle  $\theta = 41.3^{\circ}$ ), (b)  $\psi = 10^{\circ}$  (inclination angle  $\theta = 46.3^{\circ}$ ), and (c)  $\psi = 20^{\circ}$  (inclination angle  $\theta = 50.9^{\circ}$ ) (the same frictional angle  $\varphi = 35^{\circ}$ ).

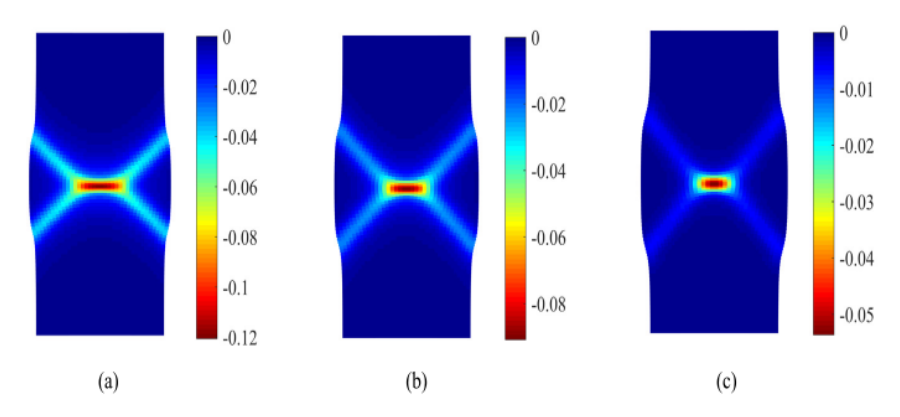


Fig. 32. Contours of the plastic volume strain assuming three dilatation angles: (a)  $\psi = 0^{\circ}$ , (b)  $\psi = 10^{\circ}$ , and (c)  $\psi = 20^{\circ}$  (the same frictional angle  $\varphi = 35^{\circ}$ ).

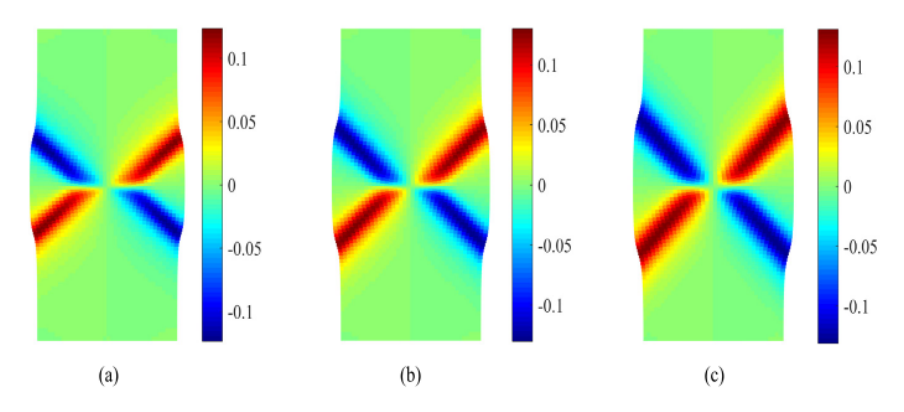


Fig. 33. Contours of the micro rotation (rad) assuming three dilatation angles: (a)  $\psi=0^{\circ}$ , (b)  $\psi=10^{\circ}$ , and (c)  $\psi=20^{\circ}$  (the same frictional angle  $\varphi=35^{\circ}$ ).

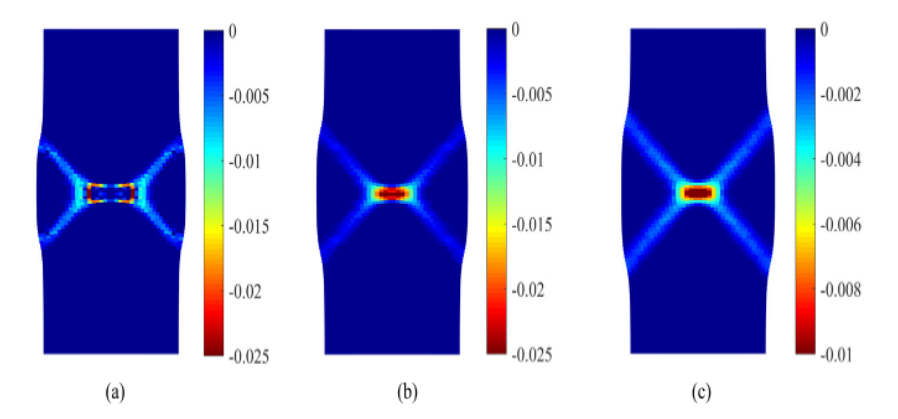


Fig. 34. Contours of the second order work assuming three dilatation angle: (a)  $\psi = 0^{\circ}$ , (b)  $\psi = 10^{\circ}$ , and (c)  $\psi = 20^{\circ}$  (the same frictional angle  $\varphi = 35^{\circ}$ ).

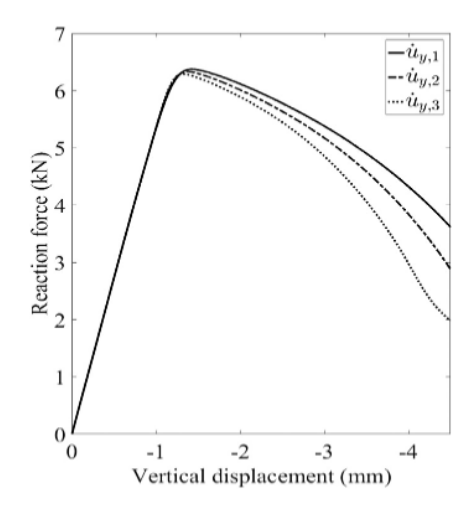


Fig. 35. Loading curves from three loading rates,  $\dot{u}_{y,1} = 0.083$  m/s,  $\dot{u}_{y,2} = 0.067$  m/s, and  $\dot{u}_{y,3} = 0.05$  m/s.

material in the bands lost its stability. It is implied that the augmented second-order work can be used to detect the formation of shear bands through the proposed micro-polar periporomechanics framework.

## 4.4. Example 4: Crack branching under high loading rates

This example deal with the crack branching in a dry visco-elastic porous material under high loading rates through the proposed energybased cracking criterion considering the micro-rotation of material points at the crack tip. Crack branching in porous media such as clay can be related to the mechanical properties of the clay layers. When the stress in a fracture zone is high in porous materials, the material cannot dissipate the energy, and the crack starts to branch due to a small critical energy release rate  $G_c$ . The crack branching can be observed when the crack reaches the critical speed of propagation (Ožbolt et al., 2011). The inertia forces at the crack tip can prevent crack propagation when the crack propagates fast, resulting in branching. We refer to the literature (e.g., Sun et al. (2021b), Chen et al. (2020)) for a comprehensive review of crack branching and hydraulic fracturing in porous media. In this example, we study the impact of loading rates, Cosserat length scales, and initial volume fractions on crack branching. We also investigate the micro rotation of material points along the crack path in crack branching.

Fig. 40 shows the model setup for this example. The initial crack length is 50 mm, as shown in Fig. 40. The tensile stress in the vertical

direction is applied on the top and bottom boundaries by the following equations.

$$\sigma_{y} = \begin{cases} \frac{\sigma_{1}t}{t_{0}} & \text{if } t < t_{0}, \\ \sigma_{1} & \text{if } t \ge t_{0}, \end{cases}$$

$$(145)$$

where  $t_0 = 6.25$  µs, and  $\sigma_1 = 8$  MPa. A stable time step  $\Delta t = 0.025$  µs. The specimen is discretized into  $200 \times 80$  uniform material points with  $\Delta x = 0.5$  mm. The horizon size is  $\delta = 4.05 \Delta x$  (Bobaru and Zhang, 2015).

The micro-polar visco-elastic material model in Section 2 is adopted for this example. The input material parameters are summarized as follows. The solid density  $\rho^s=2650~{\rm Kg/m^3}$ , initial volume fraction  $\phi_0=0.95$ , Young's modulus  $E=35~{\rm MPa}$ , Poisson's ratio  $\nu=0.25$ , Cosserat shear modulus  $\mu_c=\mu/3$ , Cosserat length scale  $l=2~{\rm mm}$ , relaxation time  $\tau_r=100~{\rm \mu s}$ .

For this example,  $\mathcal{G}_{cr}=160$  N/m is assumed for the energy-based bond criteria. The stabilization parameters  $\mathscr{G}_1=0.1$  and  $\mathscr{G}_2=0.01$  are used.

Fig. 41 plots the applied loading-time curve. The four points shown in Fig. 41 are at times  $t_1=12.75~\mu s$ ,  $t_2=29.75~\mu s$ ,  $t_3=35~\mu s$ , and  $t_4=42.5~\mu s$ . The results of the base simulations are presented in Figs. 42 and 43. Fig. 42 plots the snapshot of the crack propagation and branching on the deformed configuration at the four loading stages. The damage variable greater than 0.35 is in red (Ha and Bobaru, 2010). The results show that at time  $t_1=12.75~\mu s$  the crack starts to grow and at time  $t_2=29.75~\mu s$  the crack start branching. Fig. 43 plots the snapshots of the contours of micro-rotation of material points in the specimen. The results in Fig. 43 show that the micro-rotation of material points is concentrated on the crack tip and crack propagation and branching paths, and its value increases with the crack growth. In what follows, we study the influence of the loading rate, the Cosserat internal length scale, and the initial volume fraction on the crack branching in this example.

# 4.4.1. Influence of loading rates

In this part, we analyze the results of crack branching under three loading rates assuming the same conditions. For the three loading rates,  $t_{0,1}=2.5~\mu s$ ,  $t_{0,2}=6.25~\mu s$ , and  $t_{0,3}=12.5~\mu s$ . For all three simulations, it is assumed that  $\phi_0=0.85$  and l=2~mm. The other material parameters are the same as the base simulation.

Table 2 summarizes the timing of the crack propagation, the beginning of crack branching, and the end of crack branching. As the loading rate increases, the times for crack growth and the start of branching decrease. Figs. 44 and 45 compare the contour of the damage variable at  $t = 42.5 \,\mu s$  and the contour of micro-rotation of material points at  $t = 35 \,\mu s$  for the three loading rates, respectively.

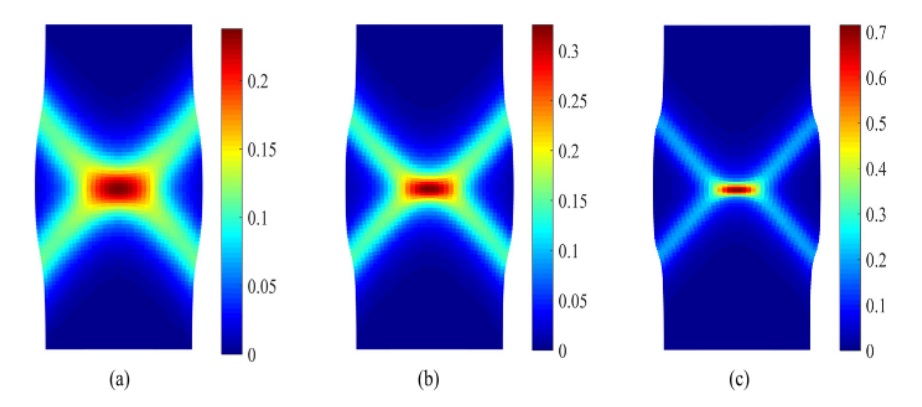


Fig. 36. Contours of the plastic shear strain from three loading rates: (a)  $\dot{u}_{y,1} = 0.083$  m/s, (b)  $\dot{u}_{y,2} = 0.067$  m/s, and (c)  $\dot{u}_{y,3} = 0.05$  m/s.

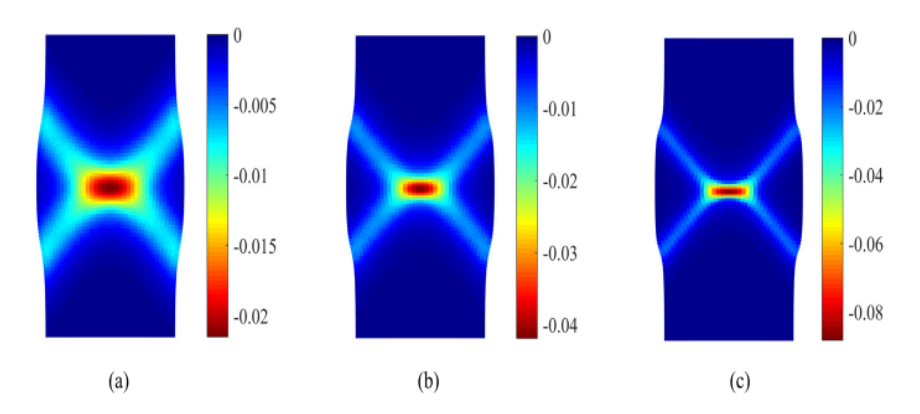


Fig. 37. Contours of the plastic volume strain from three loading rates: (a)  $\dot{u}_{y,1} = 0.083$  m/s, (b)  $\dot{u}_{y,2} = 0.067$  m/s, and (c)  $\dot{u}_{y,3} = 0.05$  m/s.

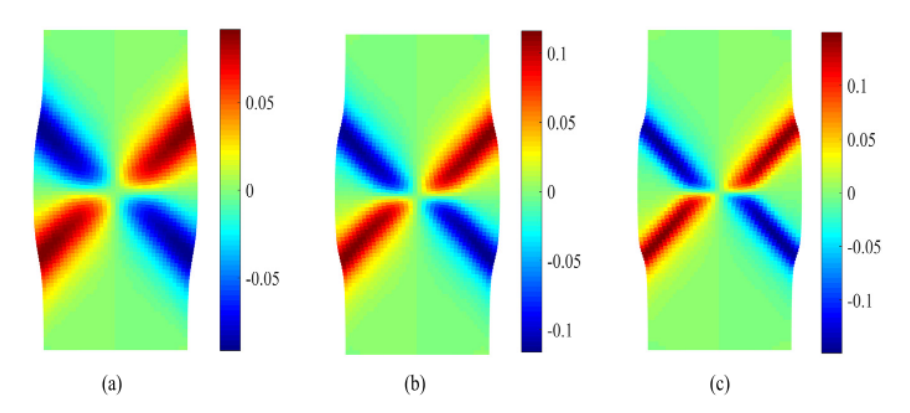


Fig. 38. Contours of the micro rotation (rad) from three loading rates: (a)  $\dot{u}_{y,1} = 0.083$  m/s, (b)  $\dot{u}_{y,2} = 0.067$  m/s, and (c)  $\dot{u}_{y,3} = 0.05$  m/s.

Table 2
Summary of the timing of crack growth and branching for the three loading rates.

t <sub>0</sub> (μs)	Start of crack growth (µs)	Start of branching (µs)	End of branching (µs)
2.5	10	26.55	50.62
6.25	12.25	28.25	53.75
12.5	16	32.75	58

#### 4.4.2. Influence of cosserat length scale

We study the impact of the Cosserat length scale on the cracking branching. The three Cosserat length scales adopted are l=1 mm, 2 mm and 3 mm. It is assumed that  $\phi_0=0.85$  and  $t_0=6.25$   $\mu$ s while the other parameters are the same as the base simulation. Table 3 summarizes the timing of crack propagation and the start and end of crack branching. The results show that the Cosserat length scale has less effect on crack propagation and branching. Figs. 46 and 47 plot the contour of the damage variable at t=42.5  $\mu$ s and the contour of the micro-rotation of material points at t=35  $\mu$ s for three cases, respectively. As shown in Fig. 47, the micro rotation of material points decreases considerably as the Cosserat length scale increases. The results in Fig. 46 show a similarity between the three cases. In contrast,

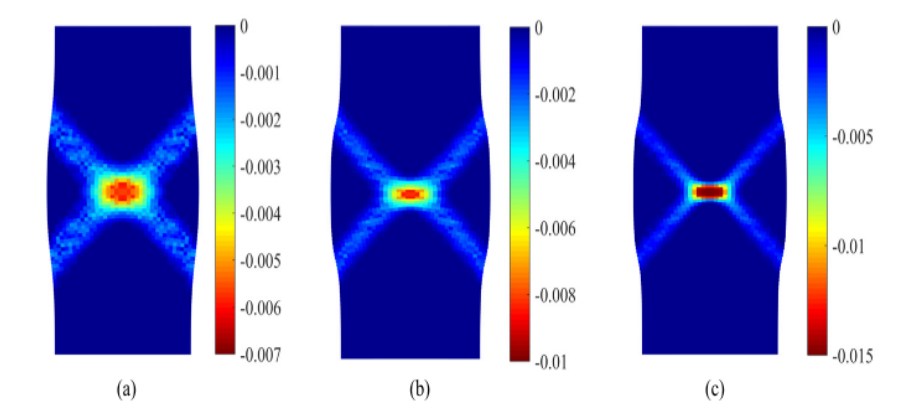


Fig. 39. Contours of the second-order work from three loading rates: (a)  $\dot{u}_{y,1} = 0.083$  m/s, (b)  $\dot{u}_{y,2} = 0.067$  m/s, and (c)  $\dot{u}_{y,3} = 0.05$  m/s.

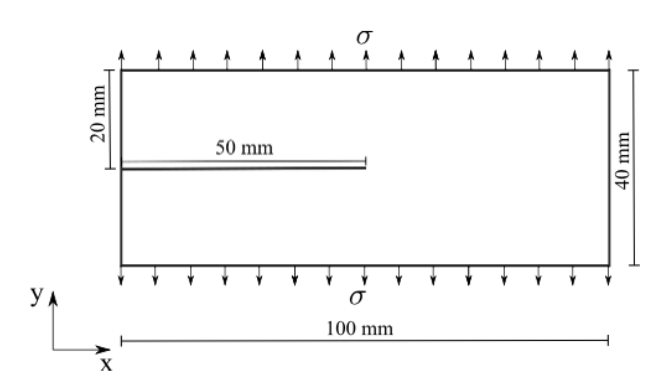


Fig. 40. Model setup for example 4.

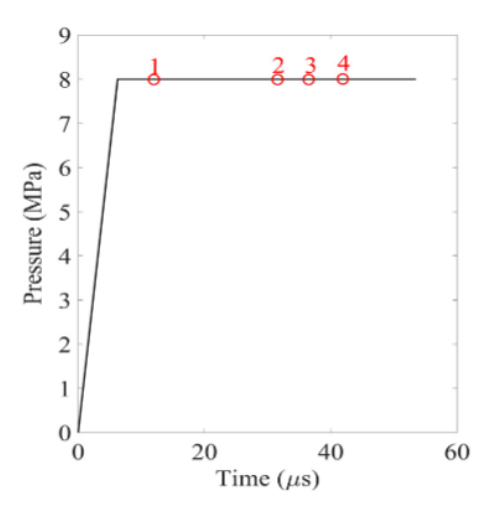


Fig. 41. Applied load versus time.

the simulations with a larger Cosserat length scale show that the crack branching advances further from the initial branching point. This may be due to the same horizon size adopted for the three simulations.

Table 3
Summary of the timing of crack growth and branching for different Cosserat length scales.

l(mm)	Start of growth (μs)	Start of branching (µs)	End of branching (µs)
1	12.25	28.5	55.5
2	12.25	28.25	52.75
3	12.12	28.12	48.75

To show the impact of the horizon on the cracking branching, we present the results of the two simulations with different horizons, i.e.,  $\delta=2$  mm and 2.5 mm, and the same Cosserat length scale,  $\mathit{l}=1$  mm. It is assumed that  $\phi_0=0.85$  and  $\mathit{t}_0=6.25~\mu s$ . The other parameters remain the same as for the base simulation. The results are shown in Figs. 48 and 49. Fig. 48 plots the contours of the damage variable at t = 42.5  $\mu s$  for the two simulations. Fig. 49 presents the contours of the micro-rotation at t = 35  $\mu s$  for the two simulations. Fig. 48 shows that the horizon affects crack propagation and branching. For the simulation with  $\delta=2$  mm, the crack propagates at time t = 12.25  $\mu s$  and starts branching at time t = 28.5  $\mu s$ . For the simulation with  $\delta=2.5$  mm, the crack propagates at time t = 12.75  $\mu s$  and starts branching at time t = 29.25  $\mu s$ . It is implied from the results that increasing the horizon could delay the branching time. The results in Fig. 49 show that the horizon has no significant effect on the magnitude of micro-rotation.

# 4.4.3. Influence of the initial volume fraction

This part analyzes how the initial volume fraction can affect the crack branching. Three initial volume fractions considered are 0.75, 0.85, and 0.95. It is assumed that  $l=2\,\mathrm{mm}$  and  $t_0=6.25\,\mu\mathrm{s}$  and the other parameters remain the same as the base simulation. Table 2 summarizes the timing of crack propagation and branching. It can be concluded from the results in Table 2 that the increase of the initial volume fraction of the porous material demands a larger load to initiate crack growth and branching. Figs. 50 and 51 plot the contours of the damage variable at  $t=42.5\,\mu\mathrm{s}$  and the contours of the micro rotation of material points at  $t=35\,\mu\mathrm{s}$  for the three cases, respectively. As indicated by the results in Figs. 50 and 51, the model with the largest initial volume fraction generates the smallest crack propagation and branching and the micro-rotation of material points around the crack (see Table 4).

#### 5. Closure

In this article, we formulate a Cosserat periporomechanics paradigm (CPPM) for modeling shear banding and cracking in dry porous media.

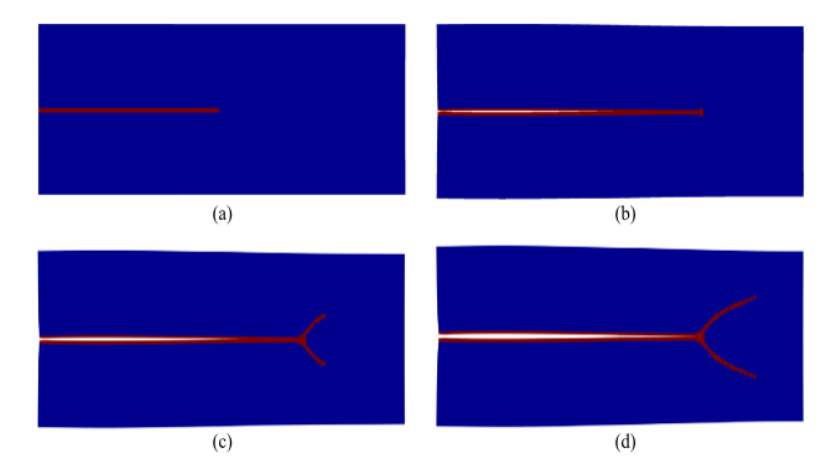


Fig. 42. Contours of the crack path on the deformed configurations (magnification factor = 10) at (a)  $t_1$  =12.75  $\mu$ s, (b)  $t_2$  =29.75  $\mu$ s, (c)  $t_3$  =35  $\mu$ s, and (d)  $t_4$  =42.5  $\mu$ s.

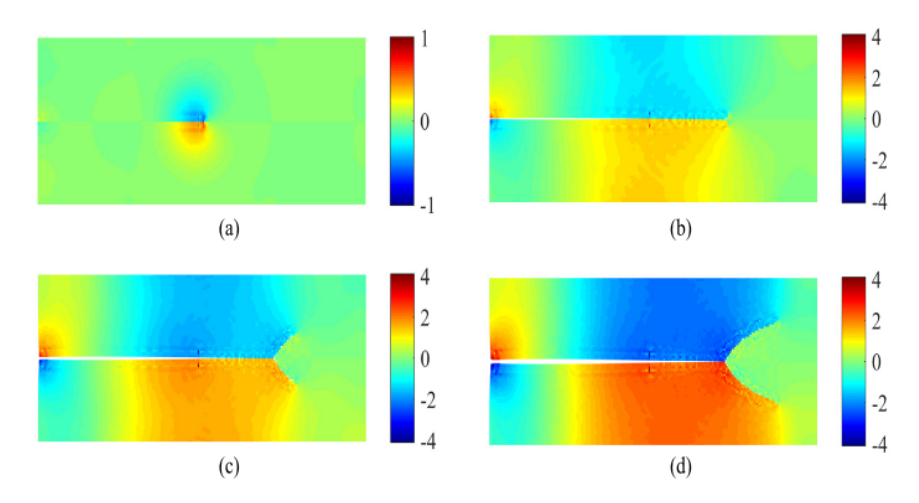
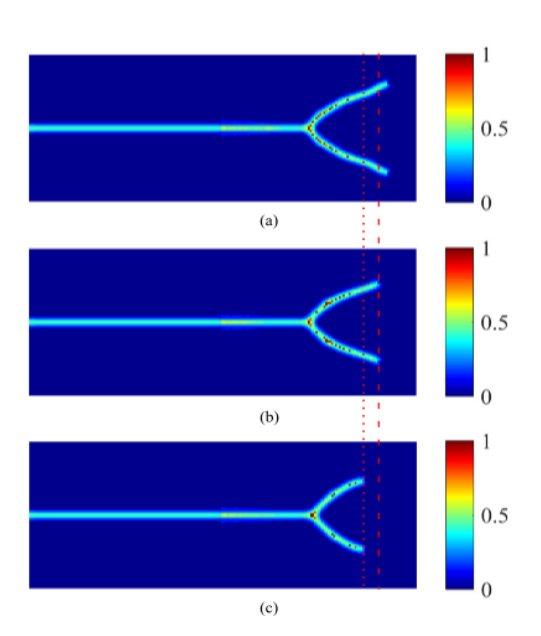


Fig. 43. Contours of the micro rotation (0.001 rad) on the deformed configurations (magnification factor = 10) at (a)  $t_1$  =12.75 μs, (b)  $t_2$  =29.75 μs, (c)  $t_3$  =35 μs, and (d)  $t_4$  =42.5 μs.



**Fig. 44.** Contours of the damage variable at  $t=42.5~\mu s$  for three loading rates: (a)  $t_{0,1}=2.5~\mu s$ , (b)  $t_{0,2}=6.25~\mu s$ , and (c)  $t_{0,3}=12.5~\mu s$ . Note: the vertical dashed lines are plotted to compare the difference of crack branching.

Table 4
Summary of the timing of crack growth and branching for three initial volume fractions

initial volume fractions.					
$\phi_0$	Start of growth (µs)	Start of branching (µs)	End of branching (µs)		
0.75	11.62	26.75	49.5		
0.85	12.25	28.25	52.75		
0.95	12.75	29.75	55		

In CPPM, a micro-structure based length scale, i.e., the Cosserat length scale, is incorporated. In this micro-periporomechanics paradigm, each material point has both translational and rotational degrees of freedom as in the Cosserat continuum theory. The two field equations consisting of the force balance equation and the moment balance equation are cast using the effective force state and moment state. The energy method is used to formulate the Cosserat periporomechanics correspondence principle for incorporating the classical micro-polar viscoplastic and viscoelastic constitutive models. We have demonstrated that the Cosserat periporomechanics correspondence principle inherits zero-energy mode instability. To circumvent this stability issue, we formulate a stabilized Cosserat constitutive correspondence principle through which classical micro-polar material models for porous media can be used directly in CPPM. This new periporomechanics paradigm has been numerically implemented through an explicit Lagrangian meshfree algorithm for modeling dynamic failure in dry porous media. Numerical examples are

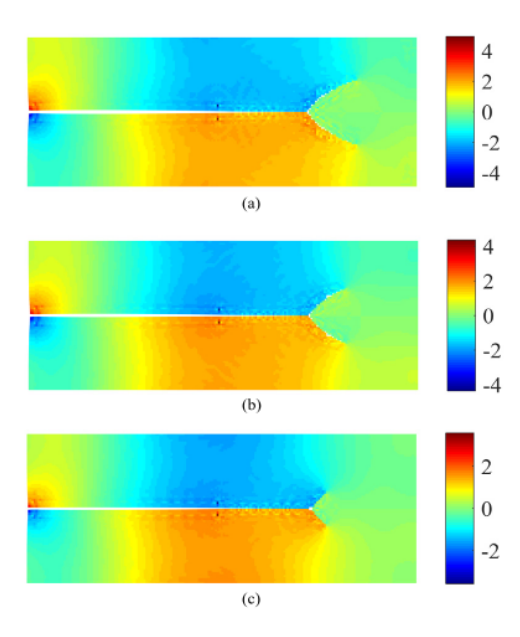


**Fig. 45.** Contours of the micro rotation ( $\times 1^{-3}$  rad) at  $t=35~\mu s$  for three loading rates: (a)  $t_{0,1}=2.5~\mu s$ , (b)  $t_{0,2}=6.25~\mu s$  and (c)  $t_{0,3}=12.5~\mu s$ .

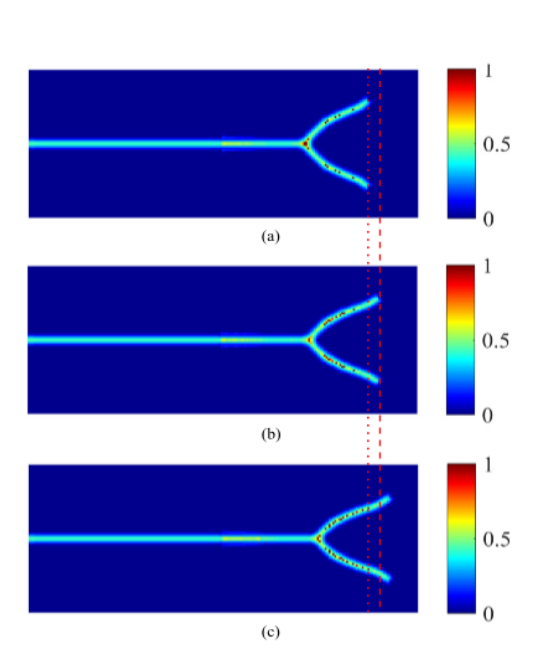


**Fig. 46.** Contours of the damage variable at  $t=42.5~\mu s$  for three Cosserat length scales: (a)  $l_1=1~\text{mm}$ , (b)  $l_2=2~\text{mm}$ , and (c)  $l_3=3~\text{mm}$ .

presented to validate the computational Cosserat periporomechanics paradigm in modeling shear bands and mode-I cracks and demonstrate its efficacy in modeling dynamic shear banding and crack branching in dry porous media. In this study, the classical second-order work criterion for detecting material instability is enhanced to incorporate micro-rotations of material points and is utilized to validate the numerical results of shear banding. Through the numerical examples, we have analyzed the factors that can impact the dynamic shear banding and

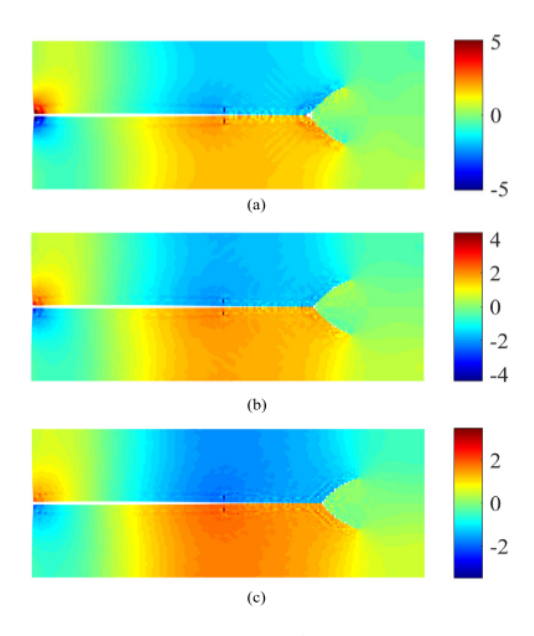


**Fig. 47.** Contours of the micro rotation  $(\times 1^{-3} \text{ rad})$  at  $t = 35 \,\mu\text{s}$  for three Cosserat internal length scales: (a)  $l_1 = 1 \,\text{mm}$ , (b)  $l_2 = 2 \,\text{mm}$ , and (c)  $l_3 = 3 \,\text{mm}$ .

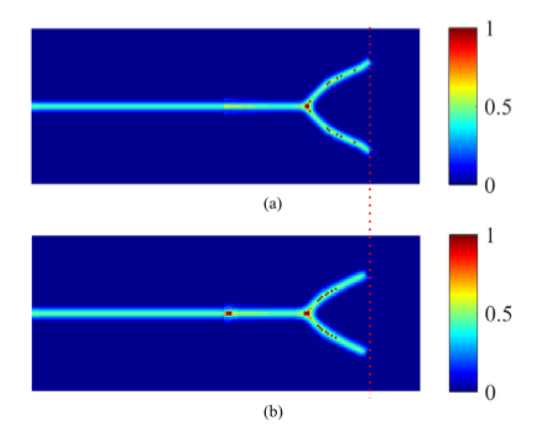


Fig. 48. Contours of the damage variable at t = 42.5  $\mu s$  for the simulations with (a)  $\delta$  = 2 mm and (b)  $\delta$  = 2.5 mm.

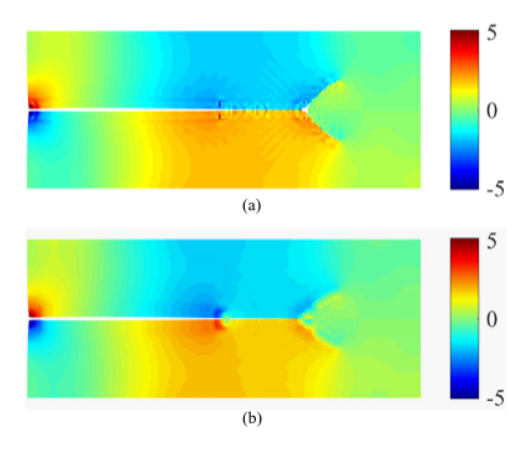
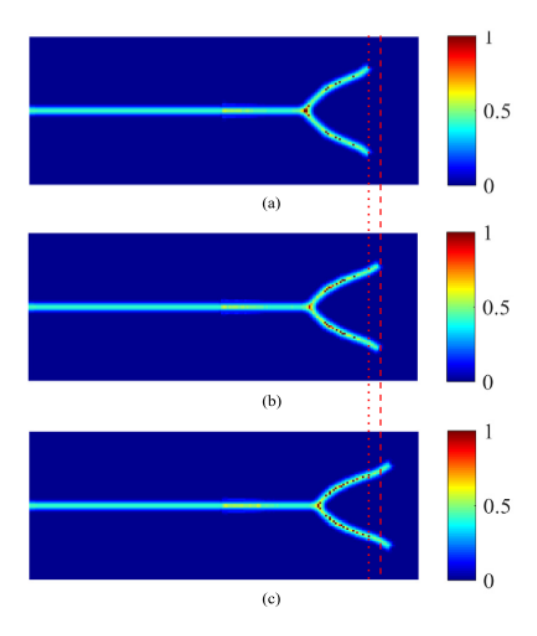
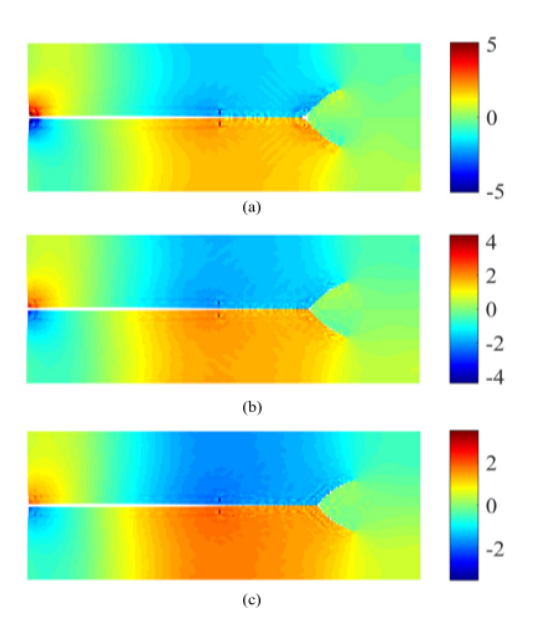


Fig. 49. Contours of the micro rotation ( $1\times10^{-3}$  rad) at  $t=35~\mu s$  for the simulations with (a)  $\delta=2$  mm and (b)  $\delta=2.5$  mm.



**Fig. 50.** Contours of the damage variable at  $t=42.5~\mu s$  for three initial volume fractions: (a)  $\phi_{0,1}=0.95$ , (b)  $\phi_{0,2}=0.85$ , and (c)  $\phi_{0,3}=0.75$ .



**Fig. 51.** Contours of the micro rotation of material points ( $\times 1^{-3}$  rad) at  $t = 35 \,\mu s$  for three initial volume fractions: (a)  $\phi_{0,1} = 0.95$ , (b)  $\phi_{0,2} = 0.85$ , and (c)  $\phi_{0,3} = 0.75$ .

crack branching in dry porous media, such as loading rates, Cosserat length scales, and initial volume fractions.

# CRediT authorship contribution statement

Xiaoyu Song: Conceptualization, Formal analysis, Funding acquisition, Investigation, Methodology, Resources, Software, Supervision, Project administration, Validation, Visualization, Writing – original draft, Writing – review & editing. Hossein Pashazad: Conceptualization, Formal analysis, Investigation, Methodology, Validation, Visualization, Writing – original draft, Writing – review & editing, Software.

#### Declaration of competing interest

The authors declare that they have no known competing financial interests or personal relationships that could have appeared to influence the work reported in this paper.

#### Data availability

Data will be made available on request.

#### Acknowledgments

This work has been supported by the US National Science Foundation under contract number 1944009. The support is gratefully acknowledged. Any opinions or positions expressed in this article are those of the authors only and do not reflect any opinions or positions of the NSF. We thank the two anonymous reviewers for their insightful reviews of this article.

#### References

Belytschko, T., Liu, W.K., Moran, B., Elkhodary, K., 2014. Nonlinear Finite Elements for Continua and Structures. John wiley & sons.

Bobaru, F., Zhang, G., 2015. Why do cracks branch? A peridynamic investigation of dynamic brittle fracture. Int. J. Fract. 196 (1), 59–98.

Borja, R.I., 2013. Plasticity. Vol. 2. Springer.

Chen, B., Sun, Y., Barboza, B.R., Barron, A.R., Li, C., 2020. Phase-field simulation of hydraulic fracturing with a revised fluid model and hybrid solver. Eng. Fract. Mech. 229, 106928.

Chen, Z., Wan, J., Chu, X., Liu, H., 2019. Two Cosserat peridynamic models and numerical simulation of crack propagation. Eng. Fract. Mech. 211, 341–361.

Cheng, A.H.-D., 2016. Poroelasticity. Vol. 27. Springer.

Chowdhury, S.R., Rahaman, M.M., Roy, D., Sundaram, N., 2015. A micropolar peridynamic theory in linear elasticity. Int. J. Solids Struct. 59, 171–182.

Cosserat, E.M.P., Cosserat, F., 1909. Théorie Des Corps Déformables. A. Hermann et fils.

Coussy, O., 2004. Poromechanics. John Wiley & Sons.

De Borst, R., 1991. Simulation of strain localization: a reappraisal of the cosserat continuum. Eng. Comput..

de Borst, R., 1993. A generalisation of J2-flow theory for polar continua. Comput. Methods Appl. Mech. Engrg. 103 (3), 347–362.

De Borst, R., Sluys, L., 1991. Localisation in a cosserat continuum under static and dynamic loading conditions. Comput. Methods Appl. Mech. Engrg. 90 (1-3), 805–827

Diana, V., 2023. Anisotropic continuum-molecular models: A unified framework based on pair potentials for elasticity, fracture and diffusion-type problems. Arch. Comput. Methods Eng. 30 (2), 1305–1344.

Diana, V., Casolo, S., 2019. A bond-based micropolar peridynamic model with shear deformability: Elasticity, failure properties and initial yield domains. Int. J. Solids Struct. 160, 201–231.

Eringen, A.C., Eringen, A.C., 1999. Theory of Micropolar Elasticity. Springer.

Gauthier, R., Jahsman, W., 1975. A quest for micropolar elastic constants.

Gerstle, W.H., 2015. Introduction to Practical Peridynamics: Computational Solid Mechanics Without Stress and Strain. Vol. 1. World Scientific Publishing Company. Gerstle, W., Sau, N., Silling, S., 2007. Peridynamic modeling of concrete structures. Nucl. Eng. Des. 237 (12–13), 1250–1258.

Ha, Y.D., Bobaru, F., 2010. Studies of dynamic crack propagation and crack branching with peridynamics. Int. J. Fract. 162 (1), 229–244.

Hill, R., 1958. A general theory of uniqueness and stability in elastic-plastic solids. J. Mech. Phys. Solids 6 (3), 236–249.

Hughes, T.J., 2012. The Finite Element Method: Linear Static and Dynamic Finite Element Analysis. Courier Corporation.

Kakogiannou, E., Sanavia, L., Nicot, F., Darve, F., Schrefler, B.A., 2016. A porous media finite element approach for soil instability including the second-order work criterion. Acta Geotech. 11 (4), 805–825.

Lakes, R., Lakes, R.S., 2009. Viscoelastic Materials. Cambridge University Press.

Lambe, T.W., Whitman, R.V., 1991. Soil Mechanics. Vol. 10. John Wiley & Sons.

Lenci, S., Clementi, F., Sadowski, T., 2012. Experimental determination of the fracture properties of unfired dry earth. Eng. Fract. Mech. 87, 62–72.

Lewis, R.W., Lewis, R.W., Schrefler, B., 1998. The Finite Element Method in the Static and Dynamic Deformation and Consolidation of Porous Media. John Wiley & Sons.

Li, X., Tang, H., 2005. A consistent return mapping algorithm for pressure-dependent elastoplastic Cosserat continua and modelling of strain localisation. Comput. Struct. 83 (1), 1–10.

- Li, W.-J., Zhu, Q.-Z., Ni, T., 2020. A local strain-based implementation strategy for the extended peridynamic model with bond rotation. Comput. Methods Appl. Mech. Engrg. 358, 112625.
- Madenci, E., Oterkus, E., 2014. Peridynamic Theory and Its Applications. Springer.
- Malvern, L.E., 1969. Introduction to the Mechanics of a Continuous Medium. Monograph.
- Marques, S.P., Creus, G.J., 2012. Computational Viscoelasticity. Springer Science & Business Media.
- Masi, F., Stefanou, I., Vannucci, P., Maffi-Berthier, V., 2021. Thermodynamics-based artificial neural networks for constitutive modeling. J. Mech. Phys. Solids 147, 104277.
- Menon, S., Song, X., 2019. Coupled analysis of desiccation cracking in unsaturated soils through a non-local mathematical formulation. Geosciences 9 (10), 428.
- Menon, S., Song, X., 2021a. A computational periporomechanics model for localized failure in unsaturated porous media. Comput. Methods Appl. Mech. Engrg. 384, 113932.
- Menon, S., Song, X., 2021b. A stabilized computational nonlocal poromechanics model for dynamic analysis of saturated porous media. Internat. J. Numer. Methods Engrg..
- Menon, S., Song, X., 2022a. Computational coupled large-deformation periporomechanics for dynamic failure and fracturing in variably saturated porous media. Internat. J. Numer. Methods Engrg..
- Menon, S., Song, X., 2022b. Computational multiphase periporomechanics for unguided cracking in unsaturated porous media. Internat. J. Numer. Methods Engrg. 123 (12), 2837–2871.
- Menon, S., Song, X., 2022c. Updated Lagrangian unsaturated periporomechanics for extreme large deformation in unsaturated porous media. Comput. Methods Appl. Mech. Engrg. (ISSN: 0045-7825) 400, 115511.
- Menon, S., Song, X., 2022d. Computational multiphase periporomechanics for unguided cracking in unsaturated porous media. Int. J. Numer. Methods Eng. 123 (12), 2837–2871.
- Menon, S., Song, X., 2022e. Computational coupled large-deformation periporomechanics for dynamic failure and fracturing in variably saturated porous media. Int. J. Numer. Methods Eng..
- Mühlhaus, H.-B., Vardoulakis, I., 1987. The thickness of shear bands in granular materials. Geotechnique 37 (3), 271–283.
- Noda, H., Lapusta, N., 2013. Stable creeping fault segments can become destructive as a result of dynamic weakening. Nature 493 (7433), 518–521.
- Ožbolt, J., Sharma, A., Reinhardt, H.-W., 2011. Dynamic fracture of concrete-compact tension specimen. Int. J. Solids Struct. 48 (10), 1534–1543.
- Pollard, D.D., Fletcher, R.C., 2005. Fundamentals of Structural Geology. Cambridge University Press.
- Silling, S.A., 2000. Reformulation of elasticity theory for discontinuities and long-range forces. J. Mech. Phys. Solids 48 (1), 175–209.
- Silling, S.A., 2017. Stability of peridynamic correspondence material models and their particle discretizations. Comput. Methods Appl. Mech. Engrg. 322, 42–57.
- Silling, S.A., Askari, E., 2005. A meshfree method based on the peridynamic model of solid mechanics. Comput. Struct. 83 (17-18), 1526-1535.
- Silling, S.A., Epton, M., Weckner, O., Xu, J., Askari, E., 2007. Peridynamic states and constitutive modeling. J. Elasticity 88 (2), 151–184.
- Silling, S.A., Weckner, O., Askari, E., Bobaru, F., 2010. Crack nucleation in a peridynamic solid. Int. J. Fract. 162 (1), 219–227.

- Simo, J.C., Hughes, T.J., 1998. Computational Inelasticity. Vol. 7. Springer Science & Business Media.
- Sleep, N.H., Blanpied, M.L., 1992. Creep, compaction and the weak rheology of major faults. Nature 359 (6397), 687–692.
- Song, X., Khalili, N., 2019. A peridynamics model for strain localization analysis of geomaterials. Int. J. Numer. Anal. Methods Geomech. 43 (1), 77–96.
- Song, X., Menon, S., 2019. Modeling of chemo-hydromechanical behavior of unsaturated porous media: a nonlocal approach based on integral equations. Acta Geotech. 14 (3), 727–747.
- Song, X., Silling, S.A., 2020. On the peridynamic effective force state and multiphase constitutive correspondence principle. J. Mech. Phys. Solids 145, 104161.
- Song, X., Wang, K., Bate, B., 2018a. A hierarchical thermo-hydro-plastic constitutive model for unsaturated soils and its numerical implementation. Int. J. Numer. Anal. Methods Geomech. 42 (15), 1785–1805.
- Song, X., Wang, K., Ye, M., 2018b. Localized failure in unsaturated soils under non-isothermal conditions. Acta Geotech. 13, 73–85.
- Steinbrugge, K.V., Zacher, E.G., Tocher, D., Whitten, C., Claire, C., 1960. Creep on the San Andreas fault. Bull. Seismol. Soc. Am. 50 (3), 389–415.
- Sulem, J., Vardoulakis, I., 1995. Bifurcation Analysis in Geomechanics. CRC Press.
- Sun, Y., Chen, B., Edwards, M.G., Li, C., 2021a. Investigation of hydraulic fracture branching in porous media with a hybrid finite element and peridynamic approach. Theor. Appl. Fract. Mech. 116, 103133.
- Sun, Y., Edwards, M.G., Chen, B., Li, C., 2021b. A state-of-the-art review of crack branching. Eng. Fract. Mech. 257, 108036.
- Tamagnini, C., Castellanza, R., Nova, R., 2002. A generalized backward Euler algorithm for the numerical integration of an isotropic hardening elastoplastic model for mechanical and chemical degradation of bonded geomaterials. Int. J. Numer. Anal. Methods Geomech. 26 (10), 963–1004.
- Tang, H., Li, Y., Hu, Z., Song, X., 2022. Numerical simulation of strain localization through an integrated cosserat continuum theory and strong discontinuity approach. Comput. Geotech. 151, 104951.
- Tang, H., Wei, W., Song, X., Liu, F., 2021. An anisotropic elastoplastic cosserat continuum model for shear failure in stratified geomaterials. Eng. Geol. 293, 106304.
- Taylor, D.W., 1948. Fundamentals of Soil Mechanics. Vol. 66. No. 2. LWW.
- Terzaghi, K., Peck, R.B., 1948. Soil mechanics. In: Engineering Practice. John Wiley and Sons, Inc, New York.
- Terzaghi, K., Peck, R.B., Mesri, G., 1996. Soil Mechanics in Engineering Practice. John wiley & sons.
- Vardoulakis, I., Graf, B., 1985. Calibration of constitutive models for granular materials using data from biaxial experiments. Géotechnique 35 (3), 299–317.
- Wang, K., Song, X., 2020. Strain localization in non-isothermal unsaturated porous media considering material heterogeneity with stabilized mixed finite elements. Comput. Methods Appl. Mech. Engrg. 359, 112770.
- Yu, H., Chen, X., 2021. A viscoelastic micropolar peridynamic model for quasi-brittle materials incorporating loading-rate effects. Comput. Methods Appl. Mech. Engrg. 383, 113897.
- Zhu, Q.-z., Ni, T., 2017. Peridynamic formulations enriched with bond rotation effects. Int. J. Eng. Sci. 121, 118–129.
- Zienkiewicz, O.C., Chan, A., Pastor, M., Schrefler, B., Shiomi, T., 1999. Computational Geomechanics. Vol. 613. Citeseer.
- Zoback, M.D., 2010. Reservoir Geomechanics. Cambridge University Press.